Effects of Temperature and Fuel Dilution on Soot Yields in an Inverted Gravity Flame Reactor

Eric Molnar

A thesis

submitted in partial fulfillment of the

requirements for the degree of

Master of Science in Engineering

University of Washington

2019

Committee:

Igor Novosselov, Chair

Philip Malte

John Kramlich

Program Authorized to Offer Degree:

Department of Mechanical Engineering

University of Washington

Abstract

Effects of Temperature and Fuel Dilution on Soot Yields in an Inverted Gravity Flame Reactor

Eric Molnar

Chair of the Supervisory Committee:
Professor Igor Novosselov
Department of Mechanical Engineering

Inverted laminar co-flow diffusion flames varied by dilution and preheat are characterized by temperature and soot emission measurements. Flame conditions vary by fuel structure (ethane, ethylene, methane), fuel dilution with Ar (0-90%), and preheat of reagents. The measured maximum flame temperature (T_{max}) is negatively correlated with dilution. Soot yields are inversely proportional to dilution and positively correlated with maximum flame temperature. The organic carbon (OC) content of soot is positively correlated with dilution and negatively correlated with temperature. T_{max} is a suitable overall combustion metric, however detailed soot analysis benefits from using a flame front temperature value closer to actual soot temperature. A peak-luminosity temperature (T_s*) is determined from flame front measurements and image analysis of soot luminosity. Generalization based on T_s* is shown to be challenging.

TABLE OF CONTENTS

LIST OF FIGURES

LIST OF TABLES

NOMENCLATURE

Notation	Definition	Units
Φ	global equivalence ratio	~
$\dot{V}$	volumetric flow rate	L/min
DR	dilution ratio	~
T_j	junction temperature of the thermocouple	K
τ_{TC}	response time of thermocouple	ms
T_g	gas temperature	K
Nu	Nusselt number	~
Re	Reynolds number	~
k_g	gas conductivity	W/m·K
d_j	diameter of thermocouple junction	m
ε	emissivity	~
σ	Stefan-Boltzman constant $(5.670 * 10^{-8})$	$W/m^2 \cdot K^4$
T_{ad}	adiabatic equilibrium temperature	K
T_{max}	measured maximum flame temperature	K
T_s*	peak luminosity temperature	K
(r, z)	coordinates of axisymmetric flame	mm
E_{corr}	Radiation correction error	K
E_r	Radial temperature gradient error	K
E_z	Axial peak-luminosity error	K

ACKNOWLEDGMENTS

Thank you to Professor Igor Novosselov for providing the opportunity, funds, and mentorship that made this thesis work possible.

Thank you to the members of my thesis committee, Professor Philip Malte and Professor John Kramlich -- for their time and evaluation of my work.

I am thankful for the opportunity to work with Justin Davis and Gaurav Mahamuni. Their Ph.D. research motivated much of my investigation into temperature measurement, and I am honored to assist in their work.

Thank you to the physics faculty at Bellevue College for their inspiration and support.

DEDICATION

To my friends and family who continue to inspire me.

Chapter 1. INTRODUCTION

Soot is a combustion generated pollutant primarily composed of black carbon. Soot emissions impact the environment by contributing to global warming and raising the surface temperature of ice caps [1, 2]. Exposure to aerosol soot particles leads to respiratory illness and soot contains known carcinogenic compounds [3, 4]. Understanding the mechanisms of soot formation provides engineering pathways for reducing anthropogenic soot emissions. Diffusion flames, i.e. combustion limited by reactant mixing rate, are typically seen in industry (e.g., diesel engines and jet turbines) [5]. In diffusion flames, soot forms in the fuel-rich region where limited oxygen prevents complete conversion reactants to products. Nucleation, growth, and oxidation of soot particles are kinetically and thermodynamically controlled behaviors depending on pressure, chemical structure, species concentration, and temperature. Soot precursors form between 1000 and 2000 K, possibley at temperatures near 1650 K [5, 6]. The residence time and temperature history of a soot particle is a promising predictor of final composition and structure [7, 8]. Characterizing diffusion flames by temperature is necessary for soot analysis. This work presents and interprets temperature measurements and soot emission data of 25 inverted laminar co-flow diffusion flames.

Upflow co-flow reactors are frequently used in soot research and are well characterized [5, 7, 9-15]. A co-flow flame reactor produces an axisymmetric diffusion flame from a fuel inlet and a co-annular oxidizer inlet. An inverted gravity flame reactor (IGFR), first reported by Stipe et al., generates a co-flow diffusion flame in the positive gravity (+g) direction [16]. The opposing convective and buoyant forces of an IGFR reduces axial acceleration and increases particle residence time within the flame. The design of the IGFR allows tunable particle diameters and facilitates soot aggregation studies [16-19]. The study of flames generated by an IGFR has furthered research into soot particle nanostructure [16, 17]. The IGFR is observed to generate a stable flame at higher dilution and lower temperature flame conditions than is possible with the reactor in an upright configuration. Convective and buoyant forces are not always aligned in practical combustions systems, therefore, similar to microgravity (i.e. non-buoyant) flames, inverted flames expand the field of soot formation research.

Temperature measurement of combustion systems can be accomplished in a number of ways. Thermocouples are an effective and low-cost temperature diagnostic tool in thermometry. As an intrusive method, probing the flame with a thermocouple introduces error, e.g., energy balance correction and flow perturbation [18, 19]. Currently, non-intrusive and semi-intrusive optical methods for measuring temperature and soot concentration are more frequently used in combustion research [10, 12, 13, 20]. Optical methods include pyrometry (single and multiwavelength measurements), Laser Light Incandescence (LLI), Spectral Soot Emission (SSE), and Laser Extinction (LE) Measurements. Charge-couple device (CCD) camera sensors have effectively determined spatially resolved measurements of soot volume fraction and temperature through windows in diesel engines [21, 22]. The quartz tube of the IGFR makes the implementation of optical methods challenging. Optical distortion due primarily to tube curvature makes thermocouple measurements the best option.

Characterizing flame conditions by measurement of the maximum flame temperature, T_{max}, is a repeatable method similar to characterization by adiabatic temperature [23]. Observation of flame luminosity, i.e. soot incandescence, reveals the greatest concentration of soot is not located at the axial position of maximum temperature. Measurements of upflow co-flow flames confirm the soot volume fraction and temperature discrepancy [10, 20, 24]. An alternative temperature metric for flame conditions is explored using image analysis of soot luminosity. The novel temperature metric is determined by identifying the flame front temperature at peak red-spectrum luminosity, i.e. maximum soot radiation. To summarize, this work evaluates fuel-to-soot conversion (soot emission factor), carbon-to-soot conversion (carbon conversion factor), and organic carbon ratio (OC/TC) with measured maximum temperature, T_{max}. Peak-luminosity temperature, T_s*, is evaluated as an alternative metric.

Chapter 2. METHODS

2.1 INVERTED GRAVITY FLAME REACTOR SETUP

Figure 2.1 illustrates the IGFR set-up. The combustion chamber boundary is 3 mm thick clear fused quartz tubing with a length of 150 mm and an inner diameter (ID) of 32 mm. Premixed fuel and argon flow through a center inlet of 3/8” steel tube (ID 7.747 mm, OD 9.525 mm). Air is stabilized by a porous mesh flow straightener before entering the combustion chamber through a co-annular inlet. The fuel tube extends 5 mm beyond the plane of the air inlet. An electric arc lighter inserted from the base of the reactor ignites the flame. Filters for soot collection sit in a removable 47 mm diameter filter housing below the exhaust manifold of the reactor. A rate adjustable vacuum pump pulls flow through the filter housing and filter. During sample collection, make-up air enters the system below combustion to maintain atmospheric conditions.

Volumetric flow of fuel, argon, and compressed lab air is controlled by glass tube flowmeters (rotameters) into the co-annular inlets of the combustion chamber. Rotameters are calibrated via soap-bubble technique (Gillibrator) before the experiment. Target volumetric dilution ratio, *DR*, determines argon flow rates.

$$DR = \frac{\dot{V}_{Ar}}{\dot{V}_{Ar} + \dot{V}_{fuel}} \qquad 2.1$$

Argon dilution is identified as a percentage and ratio interchangeably. Fuel flow rate is constant (0.12 slpm for ethane and ethylene, 0.24 slpm for methane). Air flow rate is held constant at 2.72 slpm, producing laminar flame conditions and constant equivalence ratios for each fuel in the overventilated ($\Phi < 1$) regime. The reactor used in this study is described in previous work [17].

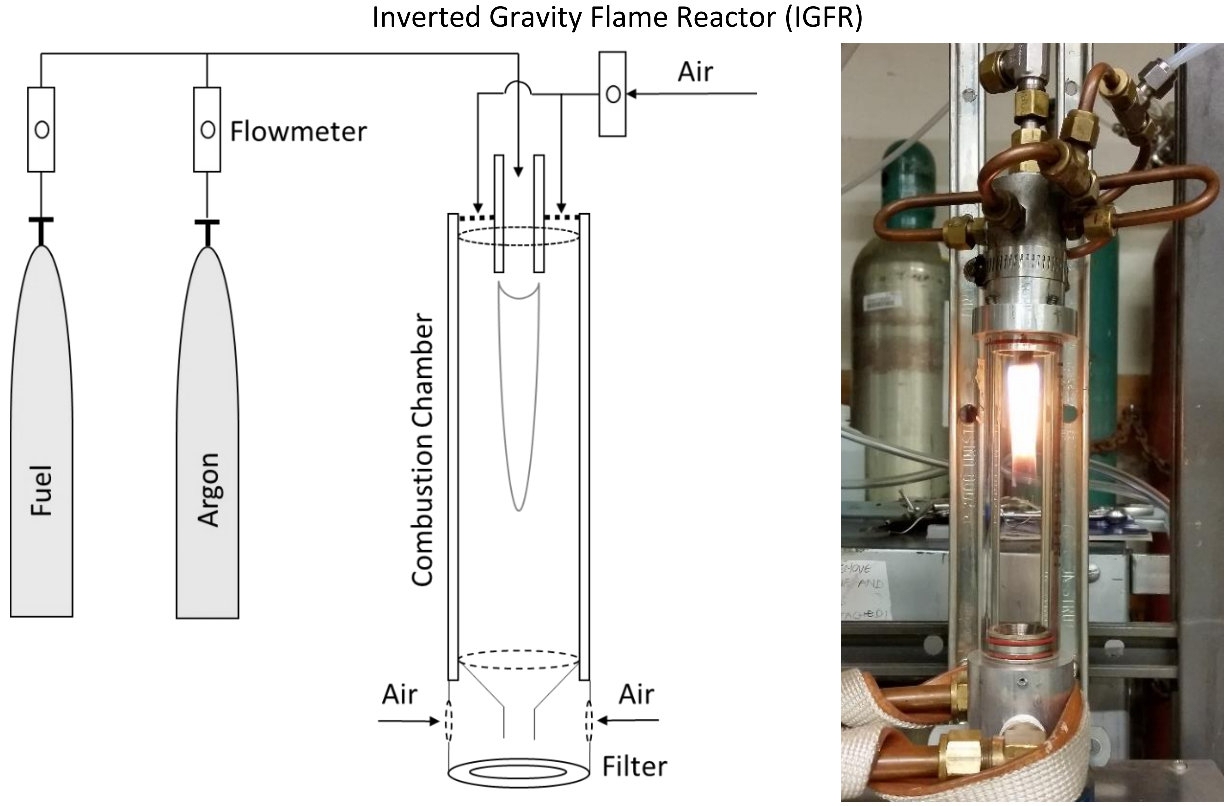

Figure 2.1. IGFR experimental set-up. Fuel and argon enter the combustion chamber via center inlet. Air enters combustion chamber via co-annular inlet. A vacuum pump pulls flow through the filter at a higher rate than total inlet flow. Flame is at atmospheric pressure, i.e. the difference in flow rate is made up by particle-free air entering exhaust manifold.

2.1.1 *Experimental Conditions*

Table 2.1 outlines the flame conditions examined this work. The hydrocarbon fuels used are compressed gas cylinders of ethane (*Airgas* 98.5% pure), ethylene (*Praxiar* 99.5% pure), and methane (*Praxair* 99.0% pure). The dilution ratio for all conditions is determined by argon flowrate as discussed (2.1). Dilution ratio values are chosen for consistency with additional research activities involving the IGFR [20]. Flow rates maintain laminar flame conditions for all experiments.

Table 2.1. Experimental Flame Conditions

Experiment	Fuel	Argon Dilution	Fuel Flow Rate (slpm)	Argon Flow Rate (slpm)	Air Flow Rate (slpm)	Inlet Temperature Condition
1	Ethane	0%	0.12	0.00	2.72	
2	Ethane	50%	0.12	0.12	2.72	
3	Ethane	67%	0.12	0.24	2.72	
4	Ethane	80%	0.12	0.48	2.72	
5	Ethane	85%	0.12	0.68	2.72	
6	Ethane	0%	0.12	0.00	2.72	Preheat
7	Ethane	50%	0.12	0.12	2.72	Preheat
8	Ethane	67%	0.12	0.24	2.72	Preheat
9	Ethane	80%	0.12	0.48	2.72	Preheat
10	Ethane	85%	0.12	0.68	2.72	Preheat
11	Ethylene	0%	0.12	0.00	2.72	
12	Ethylene	50%	0.12	0.12	2.72	
13	Ethylene	67%	0.12	0.24	2.72	
14	Ethylene	80%	0.12	0.48	2.72	
15	Ethylene	85%	0.12	0.68	2.72	
16	Ethylene	90%	0.12	1.08	2.72	
17	Ethylene	0%	0.12	0.00	2.72	Preheat
18	Ethylene	50%	0.12	0.12	2.72	Preheat
19	Ethylene	67%	0.12	0.24	2.72	Preheat
20	Ethylene	80%	0.12	0.48	2.72	Preheat
21	Ethylene	85%	0.12	0.68	2.72	Preheat
22	Ethylene	90%	0.12	1.08	2.72	Preheat
23	Methane	0%	0.24	0.00	2.72	
24	Methane	50%	0.24	0.24	2.72	
25	Methane	67%	0.24	0.48	2.72	

Table 2.1. Experimental conditions. Ambient inlet temperature conditions are unlabeled. Preheat conditions are identified.

Cases of methane preheat were not explored in this study. Equivalence ratio, Φ, is constant for each fuel (ethane $\Phi \approx 0.74$, ethylene $\Phi \approx 0.64$, methane $\Phi \approx 0.84$ based on NIST WebBook gas density at 25 C). A Φ of less than one ($\Phi < 1$) indicates all flames are in overventilated conditions. For condition identification throughout this work, Ar dilution is referred to as a percentage or ratio following fuel (e.g. ethylene 80% or ethylene 0.80).

2.1.2 *Reactor Preheat*

Inlet flow is preheated to 500 K by insulated electric heating tape controlled by a 720-Watt controller (*OMEGALUX* 120 V HTWC101-010). The heating tape is secured around the inlet manifold and insulated with fiberglass tape (Figure 2.2-3ab). The inlet temperature, T_i, is measured by an R-type thermocouple at a consistent location near the fuel inlet until the system reaches steady state (Figure 2.2-9a). A K-type thermocouple permanently positioned in contact with the inlet manifold monitors the manifold for reference temperature during operation (Figure 2.2-4ab).

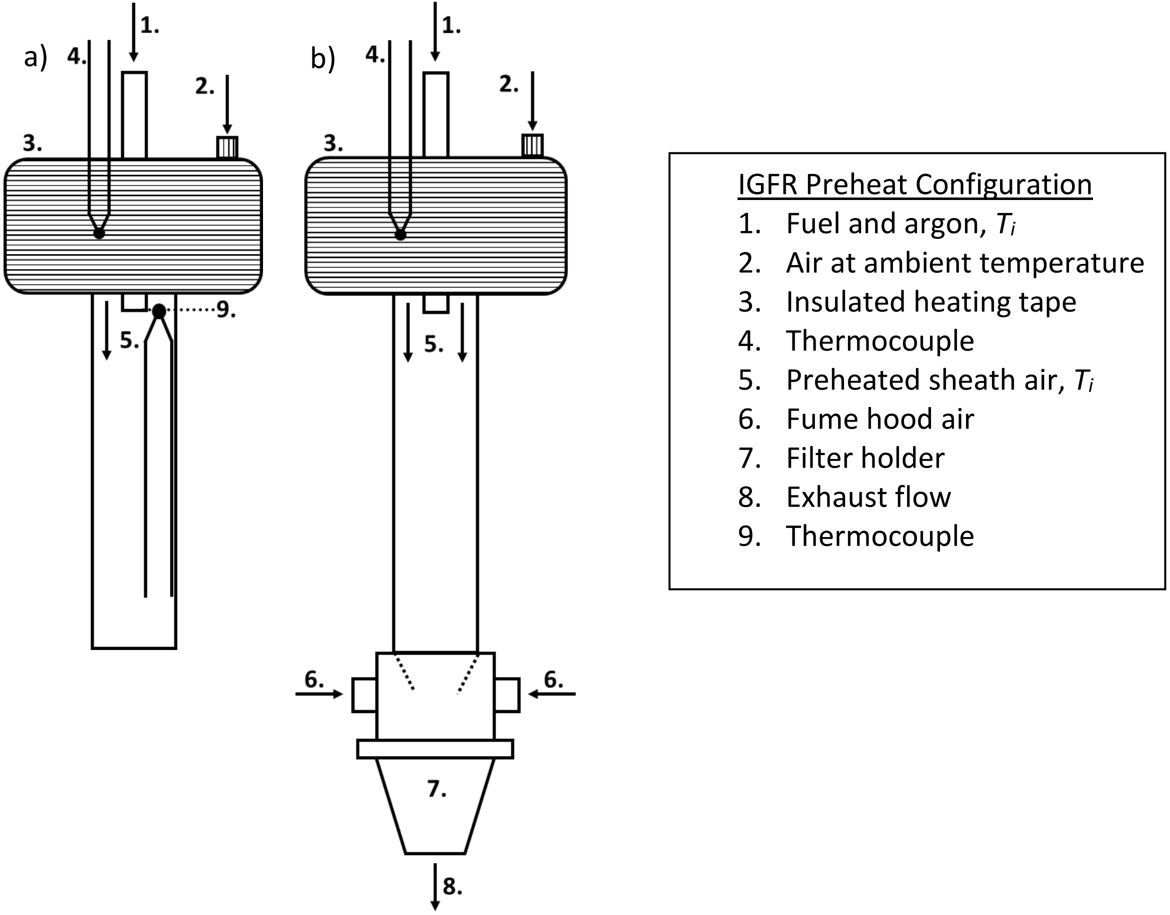

Figure 2.2. IGFR preheat set-up. System is preheated to steady-state at desired reagent temperature (a) before operation (b). A K-type thermocouple (4ab) monitors manifold temperature during temperature measurements and soot collection.

2.2 SOOT COLLECTION

Several ex-situ soot measurements are performed on soot emissions collected from IGFR flame conditions. Organic carbon ratio (OC/TC) is a chemical composition measurement made by *Sunset Laboratories Inc.* using the thermal-optical method developed for diesel exhaust [21, 22]. Organic carbon content in soot is correlated with polyaromatic hydrocarbons (PAHs) linked to cardiovascular disease. Additional techniques include gas chromatography-mass spectrometry (GC-MS) and excitation-emission matrix (EEM), a fluorescence spectroscopic technique [20]. Soot nanostructure is determined by transmission electron microscopy (TEM) [17]. Soot emission results presented in this work are limited to comparison of soot yeilds and OC/TC with maximum flame temperature and dilution.

Soot emissions are collected on porous fiber filters downstream of the reactor (Figure 2.1). The duration of the collection is recorded in minutes and ranges from 1 to 120 minutes depending on dilution ratio, i.e., low dilution flames produce more soot and require shorter collection times. The soot mass is calculated from microbalance measurements within 0.5 μg (*Mettler-Toledo UMT-2*, Greifensee, Switzerland) of filters before and after collection. The balance procedure is a standardized process that mitigates uncertainties from humidity and static electricity. Filters used with the IGFR have diameters of either 35 mm or 47 mm. Filter size and type varies with soot analysis technique. *Sterlitech* glass microfiber filters (934-AH) are used for TEM and emission factor collection. Pre-fired quartz-fiber filters are required for organic carbon measurement [21].

2.3 TEMPERATURE MEASUREMENT

Maximum flame temperature, T_{max}, is the primary flame characterization explored in this work. The measurement method is based on two fundamental assumptions of flame structure. First, the axisymmetric nature of co-flow flames reduces the temperature field dimension, i.e. temperature measurements along one side represent all azimuthal temperatures at that radial and axial position. Second, the flame front of a diffusion flame is the location of local stoichiometric mixture fraction and peak radial temperature [5]. For each flame condition, an axial profile of flame front temperatures is built from measurements at a 5 mm resolution. The maximum value of the axial profile determines T_{max}. The axial temperature profile is used to determine peak-luminosity temperature, T_s*, as explained in a later section, 2.4.

2.3.1 *Temperature Data Collection*

Flame temperature in the IGFR is measured with a bare wire thermocouple attached to a stepper motor (0.9-degree rotation per step) on a vertical stage (Figure 2.3). A microprocessor is programmed to periodically move the exposed junction of the thermocouple from the sheath air region into the flame. Thermocouple junction exposure to the flame is 2.5 seconds. The thermal response time-step, τ_{TC}, of the P13R-003 thermocouple is less than 200 ms. The duration of measurement (2.5 s) allows for thermal equilibrium while mitigating possible soot deposition. Soot deposition is minimal in the high-temperature oxidative region and at axial positions near reactor inlet. For low dilution flames and downstream positions in the flame, soot escapes the flame front boundary and soot deposition is more likely.

The frequency of measurement is limited by the acquisition module at 200 ms (*OMEGA* TC-08). The recorded value for each axial measurement along the flame front is determined from the maximum of ~10 measurements. The axial position is varied by adjusting the linear stage at 5 mm increments from the end of the fuel inlet tube to the end of the visible flame.

Thermocouple measurements are recorded by acquisition software (*PicoLog Beta 6*) in Celsius. The R-type thermocouple has a tolerance of 0.25% of measured value (e.g. 3.75 C for

1500 C). The acquisition module has an additional tolerance of 0.5 C plus 0.2% of measured value. Measurement values are converted to Kelvin before radiation correction.

Temperature Measurement Set-up

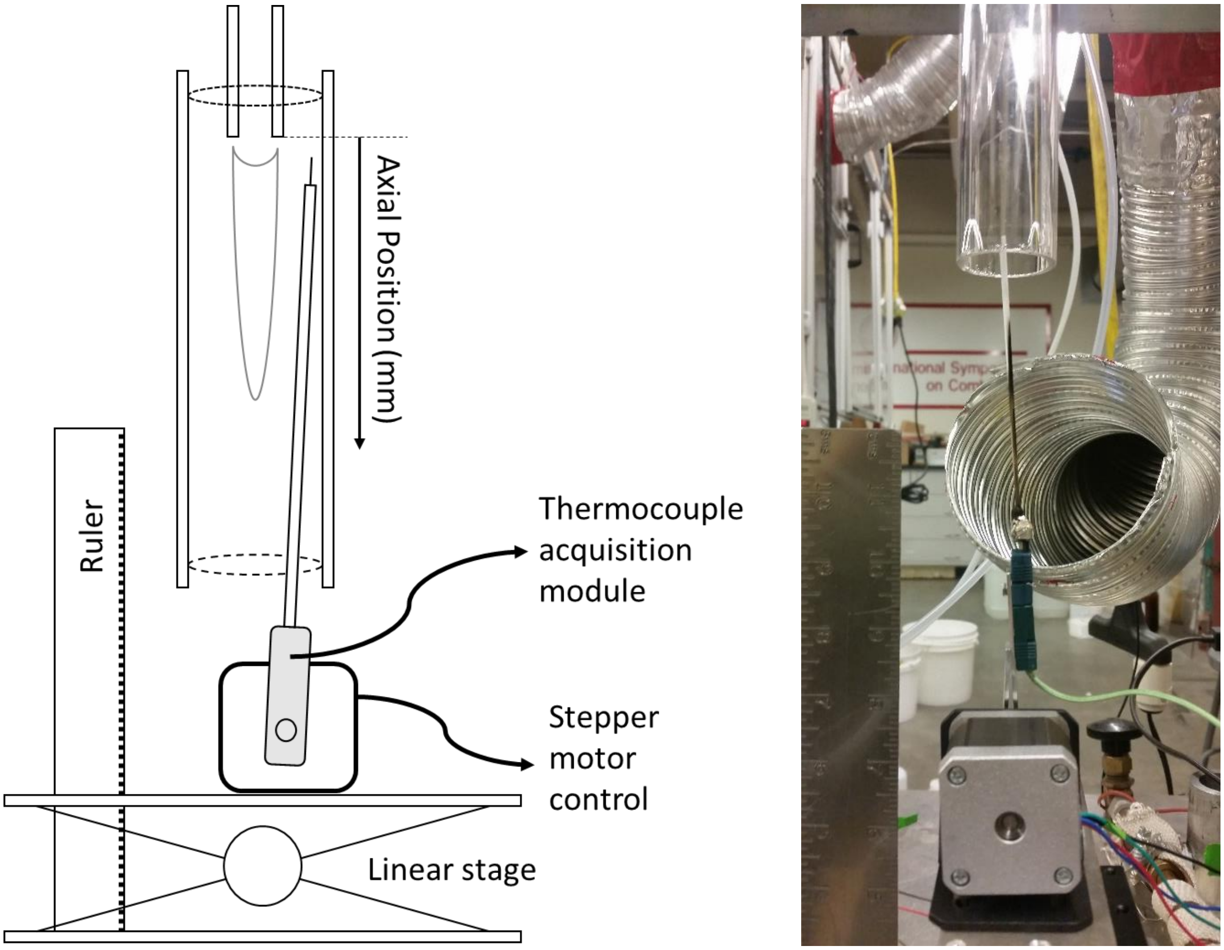

Figure 2.3. Temperature measurement set-up. Linear stage is manually positioned against a ruler to set the thermocouple junction at the desired axial position. The stepper motor is laterally positioned to make measurement of the flame front, i.e. peak radial temperature.

Spatial, i.e. two-dimentional, measurements of the temperature were tested. The repeatability in lateral positing was a challenging with current design. Additionally, probing the flame beyond the flame front produced greater flow perturbation. Flame perturbation was observed to be minimal during measurement of the flame front. Positioning the measurement system by maximum radial temperature was a reproducible method.

2.3.2 *Radiation Correction*

Bare-wire thermocouples in a hot gas environment can be affected by four modes of heat transfer: convection, radiation, conduction, and catalysis. Conduction losses can be mitigated by using a thermocouple with a sufficiently small wire diameter [23]. Catalytic effects are difficult to quantify and are not often addressed in literature [14, 24-26]. A non-catalytic coating (e.g. silica) can be applied to thermocouples, however the subsequent effect on junction diameter and emissivity challenge accurate measurements further [27]. Catalytic heating is expected when introducing platinum-based thermocouples to the reactive regions of combustion. The effect of catalysis is not quantified in this work.

A balance of radiation and convection is often assumed to account for the difference between thermocouple junction temperature, T_j, and gas temperature, T_g, [14, 23, 24, 27]. The thermocouple radiation correction is quantified by a quasi-steady-state energy balance.

$$\varepsilon_j \sigma \left(T_j^4 - T_w^4\right) = h(T_g - T_j) \qquad 2.2$$

Measurements are made with an R-type thermocouple (*OMEGA* P13R-003). R-type thermocouples have a platinum-13% rhodium wire butt-welded to a platinum wire (Figure A.15). Thermocouple junction emissivity, ε_j, is calculated from a temperature-dependent correlation (Eq. 2.3) for an S-type (Pt-Pt10%Rh) [27].

$$\varepsilon_{typeS} = -0.1 + 3.24 * 10^{-4} T_j - 1.25 * 10^{-7} T_j^2 + 2.18 * 10^{-11} T_j^3 \qquad 2.3$$

Estimation of the heat transfer coefficient, *h*, is possible with the Nusselt number, *Nu*.

$$Nu \equiv h d_j / k_g \qquad 2.4$$

Determination of Nu is challenging and important [27]. Nusselt number of a sphere (*Nu = 2*) is chosen for this work based on an assessment of Nusselt number correlations and uncertainty, the Re correction did not yield a significant change in the Nu value due to the small bead diameter.

The spherical assumption of the thermocouple junction represents a perfect sphere in a stagnant medium. Alternatively, a perfect cylinder in a stagnant medium gives a Nu of three-tenths ($Nu=0.3$). Empirically determined correlations for cylindrical and spherical Nusselt numbers require additional local property information (e.g. velocity, density and viscosity for Reynolds number). IGFR specific estimations of Nu based on correlations from literature give $Nu=0.7$ and $Nu=2.26$ for certain cylindrical and spherical correlations, respectively. Dilution is found to vary Reynolds number estimation in the range of Re~0.35-0.45. Qualifying the thermocouple junction geometry as a sphere or cylinder is important. A junction-to-wire (i.e. bead-to-wire) ratio can help determine geometry (< 2 a cylinder, > 3 a sphere) [27]. Thermocouple junction diameter, d_j, is measured at 170 μm by optical microscope. Given the bead-to-wire ratio of 2.3, a quantitative determination of sphere vs cylinder assumption is not clear. The stagnant medium spherical assumption ($Nu = 2$) results in reasonable correction values (< 200 K), is within correlation estimations, and reduces additional uncertainty from estimation of local properties. Final temperature values are accurate within the limitations of the assumptions for the radiation correction.

Gas conductivity, k_g, is assumed to be that of air and is calculated by a temperature-dependent correlation from literature [14].

$$k_g = \left(55.4T_g + 1228.9\right) * 10^{-6}\ [\mathrm{W/m \cdot K}] \qquad 2.5$$

The thermocouple junction in the IGFR balances radiative heating with two view factors: a soot region on the interior of the flame front and the quartz tube on the wall side. The radiation correction equation assumes an optically thin flame. The wall temperature, T_w, is assumed that of the inner surface of the quartz tube. Measurements of T_w at the axial positions of maximum temperature give approximately 500 K. The lowest junction temperatures measured were $T_j \approx 1200$

K; T_w shows negligible influence on the correction. Additionally, radiation correction from the preliminary results showed agreement within 25 K for R-type thermocouple junctions of 170 and 470 µm. Measurement results presented in this work are from a single 170 µm R-type thermocouple.

2.4 FLAME IMAGE ANALYSIS

Luminosity measurements of flames can spatially determine soot concentration coupled with soot temperature [28-30]. The spectral density of thermal radiation is described by Plank's radiation law.

$$I(\lambda, T) = \frac{2\pi hc^2}{\lambda^5} \frac{1}{e^{hc/\lambda k_B T} - 1} \quad 2.6$$

Where h is Plank's constant and k_B is the Boltzmann constant. As a near-ideal black body, the intensity of soot radiation follows Stefan-Boltzmann's law and has a 4th-order temperature dependence with $I(\lambda, T)$ which peaks in the infrared region as determined by Wein's displacement law. An incandescing flame is not optically thin as assumed for the radiation correction equation. Laser Extinction measurements (LEM) relies on line-of-sight extinction of a laser by soot particles to determine soot volume fraction [29]. Line-of-sight optical measurements of flames, such as luminosity imaging, are affected by the absorption, scattering, and attenuation properties of soot particles. Quantification of particle concentration is outside the scope of this work, and impractical in the current IGFR system. In this work, image analysis of flames luminosity within the visible red spectral region ($575 < \lambda < 675$ nm) is used to determine the axial location of the peak soot irradiance in the flame for estimation of peak soot concentration.

Images are captured with a Nikon DSLR 5100, CMOS-sensor digital camera [31]. Aperture (f) and sensitivity (ISO) are held constant while shutter speed is adjusted to set image exposure. A MATLAB script is used to locate the median axial position of the peak intensity of the red spectrum pixel layer. The red layer of a flame image visibly matches soot incandescence (Figure A.5), i.e., the spectral response of the light wavelengths closest to peak thermal radiation of soot (Figure A.6). Peak intensities of the RAW image format matched that of the smaller file format of jpg. Pixel distance is referenced with a ruler and with laser marks identifying a set vertical distance of 80 mm.

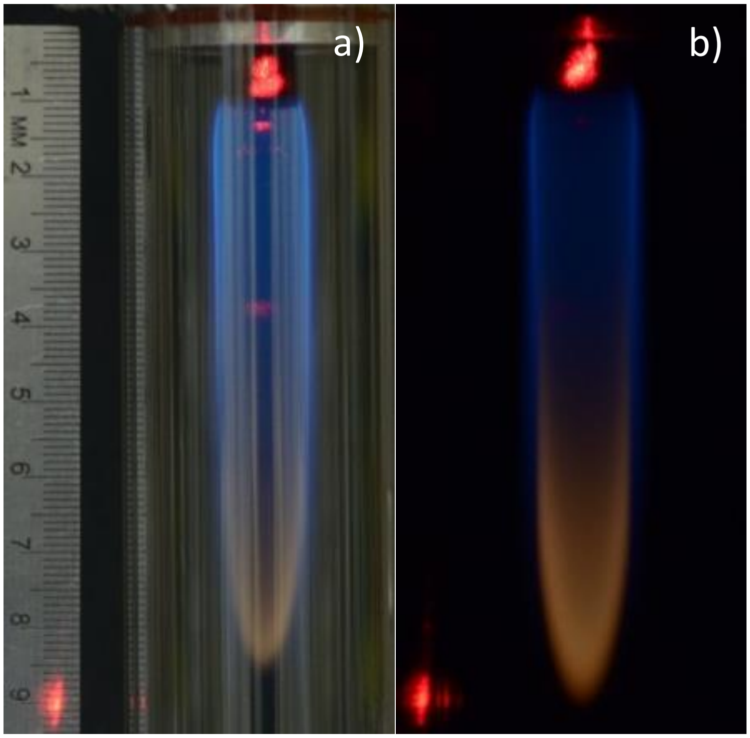
Spatial Reference for Image Pixels

Figure 2.4. Spatial reference for image pixels. A ruler measures spatially placed laser marks (a). Eliminating ambient light, laser marks identify spatial distance (b).

Maximum soot irradiance is aligned with flame front temperature measurements to determine peak-luminosity temperature, T_s*. Peak-luminosity locations between temperature data points are linearly interpolated to determine respective temperature (Figure 2.6). T_s* can be explained as the actual soot temperature, T_s, at a spatial coordinate (r, z) within the flame plus a qualified error term, E_{total}, as shown in equation 2.7.

$$T_s(r,z) = T_s^* \pm E_{total} = T_j(r^*,z) + T_{rad} + E_{corr} - E_r \pm E_z \qquad 2.7$$

All terms are in Kelvin. The total error, E_{total}, between peak-luminosity temperature, T_s*, and soot temperature, T_s, is a sum of three primary sources of error (E_{corr}, E_r, E_z). The radiation correction value, T_{rad}, is the difference between gas temperature, T_g, and junction temperature, T_j, i.e., $T_g = T_j + T_{rad}$ (Eq. 2.2). The energy balance correction error, E_{corr}, is challenging to quantify because of radiation correction assumptions (e.g., Nusselt number, correlations for emissivity and gas conductivity) and heat transfer balance assumptions (e.g. catalysis, conduction). The radial location of soot, *r*, is approximated by, *r**, the radial position at the flame front. Flame front temperatures and corresponding soot temperatures are predicted to vary as much as 300 K, based on spatially resolved measurements of similar upright flames (Figure A.13).

Radial and Axial Errors for T_s*

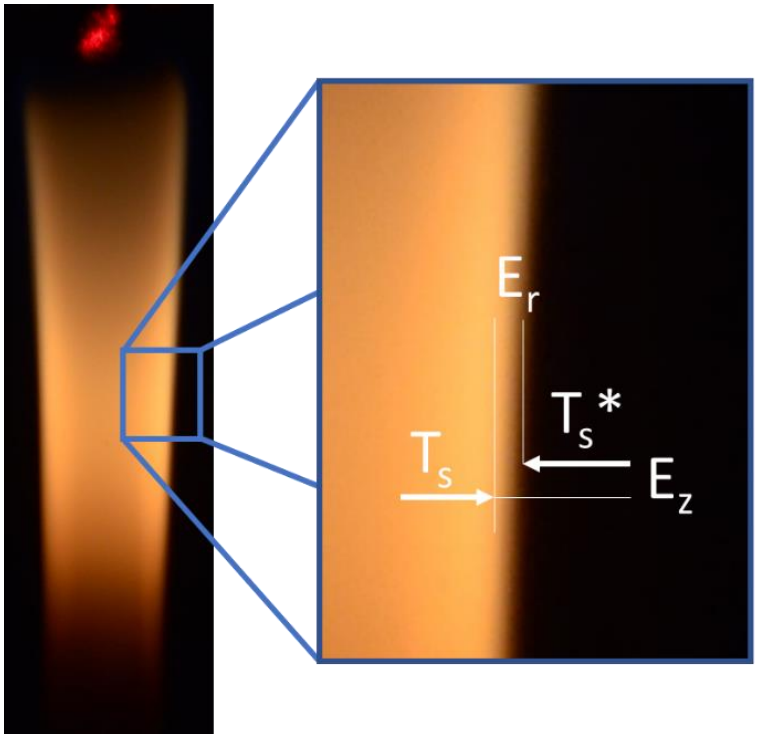

Figure 2.5. Radial and axial errors for peak-luminosity temperature. Radial error, E_r, is assumed to be negative by an axially dependent value up to 300 K, therefore T_s* only characterizes soot temperature. Axial error, E_z, is defined as the error due to the difference between peak soot radiation and maximum soot concentration. E_z is not quantified in this work.

Qualitatively, 4th-order temperature dependence of soot incandescence implies maximum soot concentration is lower in the flame than peak soot radiation. Flame front temperatures decrease axially beyond the peak temperature, radial gradients decrease axially as well. The temperature history of a soot particle following a streamline just inside the flame front will see a less drastic change in temperature then the flame front profile indicates.

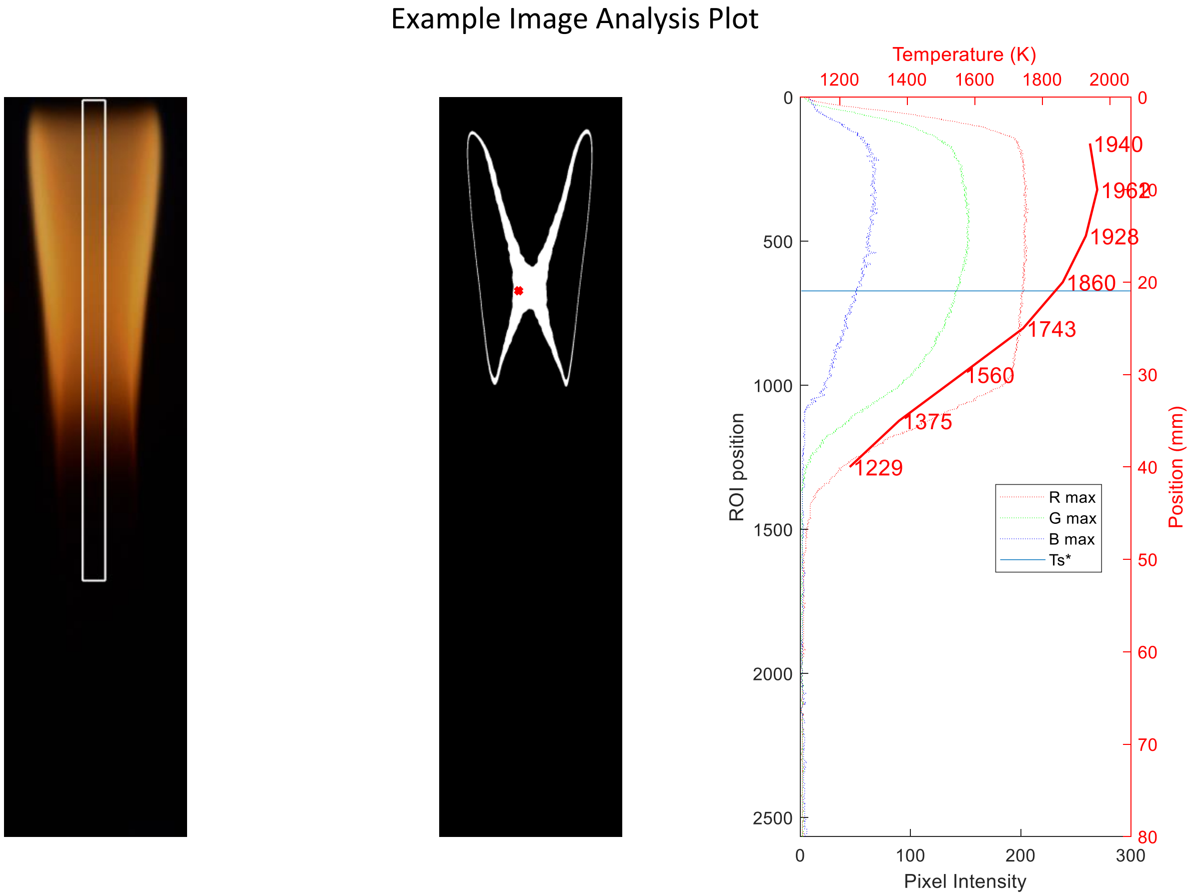

Figure 2.6. Image analysis of Ethylene 25% dilution without preheating. Selected centerline region (left) is scanned for maximum luminosity. A binary image of pixels within 5 intensity points (center) illustrate the near peak luminosity profile. Higher intensity pixels exist on wings of flame due to line-of-sight particle concentration. Relative axial concentration is independent of radial position. A red ‘x’ indicates the pixel point (center) used for correlation with measured flame front temperatures to produce T_s* (right). Temperatures are linearly interpolated between measured points.

Chapter 3. RESULTS AND DISCUSSION

3.1 MAXIMUM MEASURED TEMPERATURE

Figure 3.1 shows the measured maximum flame temperature, T_{max}, relative to argon dilution for the three fuels: ethane, ethylene, and methane. T_{max} is negatively correlated with increasing dilution. Reduction in the molecular concentration of fuel in the reaction zone is a mechanism by which dilution effects flame temperature.

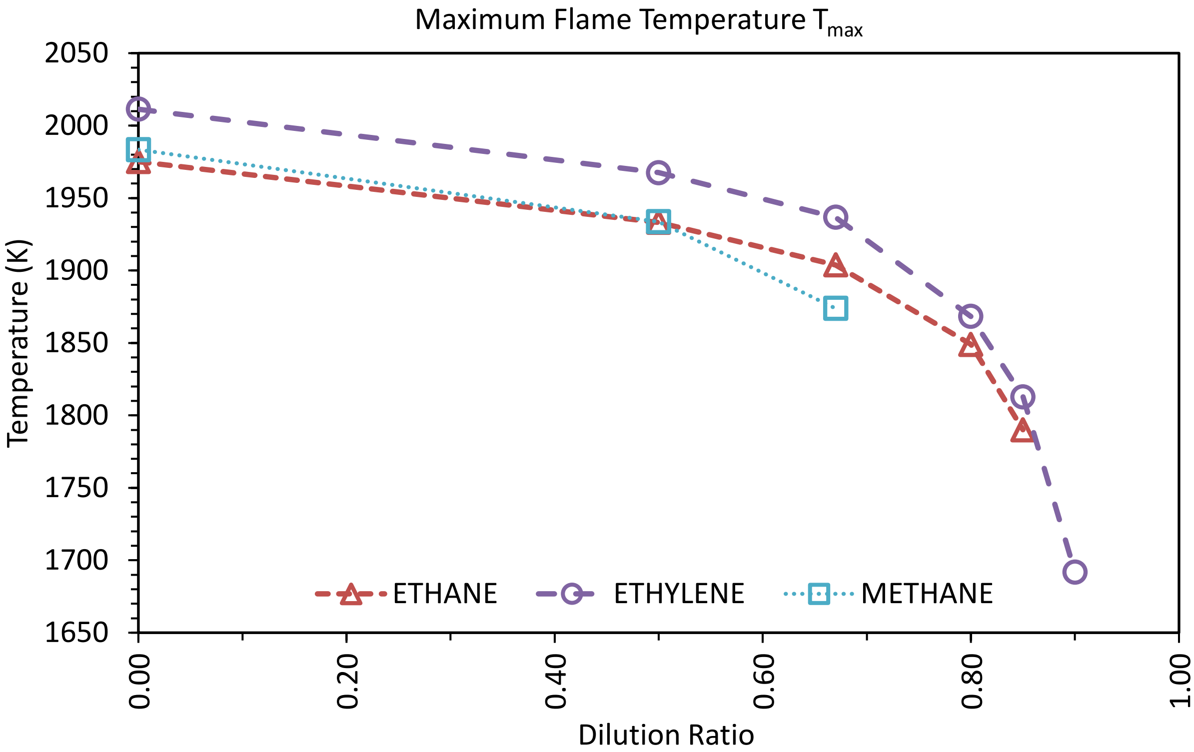

Figure 3.1. Measured maximum temperature for non-preheat conditions. Fuel flow rates and equivalence ratios are constant.

Flame temperature is a function of fuel type, initial temperature, mixture fraction, soot radiation effects, and pressure [5, 6, 30]. All conditions in the IGFR are at atmospheric pressure. IGFR maximum temperature trends are consistent with similar upright co-flow diffusion flames [10, 11, 32]. Inert gas dilution lowers fuel concentration in the reaction zone thereby limiting reaction rate, and heat generated [5]. The magnitude of the decrease in T_{max}, i.e. slope, increases at higher dilutions (e.g. 0.80 and above) as flame conditions approach extinction. The rate at which temperature decreases is different for each fuel, which supports a chemical structure unique limit at which flame extinction by diluent occurs. The maximum temperature measurements are subject to two sources of error. First, measurement device tolerance can lead to an error of ±10 K. Second, the radiation correction error that comes from model assumptions (e.g. conduction, catalysis, Nusselt number, and emissivity correlation) may lead to systematic error.

Comparison of T_{max} with adiabatic temperatures, T_{ad}, for each condition is presented in Figure 3.2. T_{ad} is determined by constant pressure and enthalpy calculation using a publicly available *STANJAN*-based chemical equilibrium calculator [33].

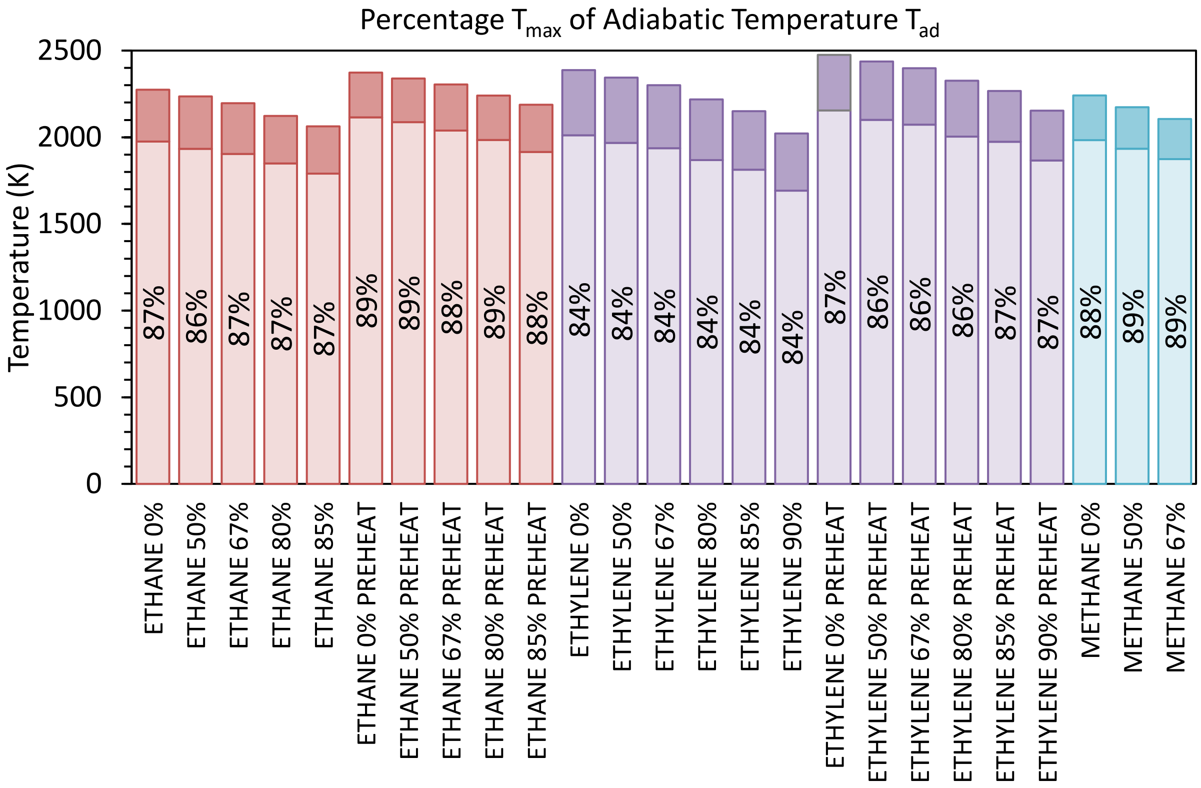

Figure 3.2. Measured maximum temperature and the adiabatic temperature. Lower columns indicate measured temperatures relative to upper columns of adiabatic temperatures. The temperature difference is explored by reporting T_{max} as a percentage of theoretical thermal equilibrium for stoichiometry of each condition.

In the combustion chamber of the IGFR, heat transfer, incomplete combustion, and dissociation leads to a lower temperature than is calculated theoretically. Soot particles have a significant role in radiative heat transfer [12]. The ranking of fuels by greatest soot yield, i.e., ethylene > ethane > methane (Figure 3.4), corresponds with the relative difference between adiabatic and measured temperatures (i.e. T_{max} = 84%, 87%, 89% of T_{ad}, relatively). Comparison of T_{max} percentages for preheating conditions shows consistency with non-preheat conditions, i.e. ethylene measured temperature percentages are approximately 2% lower than ethane. Methane 0% dilution has a higher T_{max} than ethane 0% dilution (Figure 3.1), while T_{ad} for ethane is greater methane. Soot yield results and radiative heat transfer of soot particles explains most of the measured temperature trends.

Ethane and ethylene preheat conditions have increased in soot emissions (Figure 3.8) and are observed to incandesce at greater intensity (Figure A.2). If thermal radiation loss is the primary contributor to the difference between adiabatic and measured temperatures, preheat conditions would show a greater difference than their respective non-preheat conditions. Added heat increases reaction rate. It is possible increased interaction with radicals under preheat conditions could lead to catalytic heating and elevates measured temperature. In other words, catalysis may account for the higher T_{max}/T_{ad} percentage seen in preheat conditions despite increased thermal loss expected with greater soot yield.

3.1.1 *Emission Factor*

Figure 3.3 plots soot emission factor (emission factor) as a function of T_{max}. Fuel flow rates for ethane, ethylene, and methane are 0.15, 0.14, 0.16 g/min, respectively. An emission factor is reported as milligrams soot per grams fuel. The emission factor is non-linearly correlated to T_{max} when temperature is controlled by dilution.

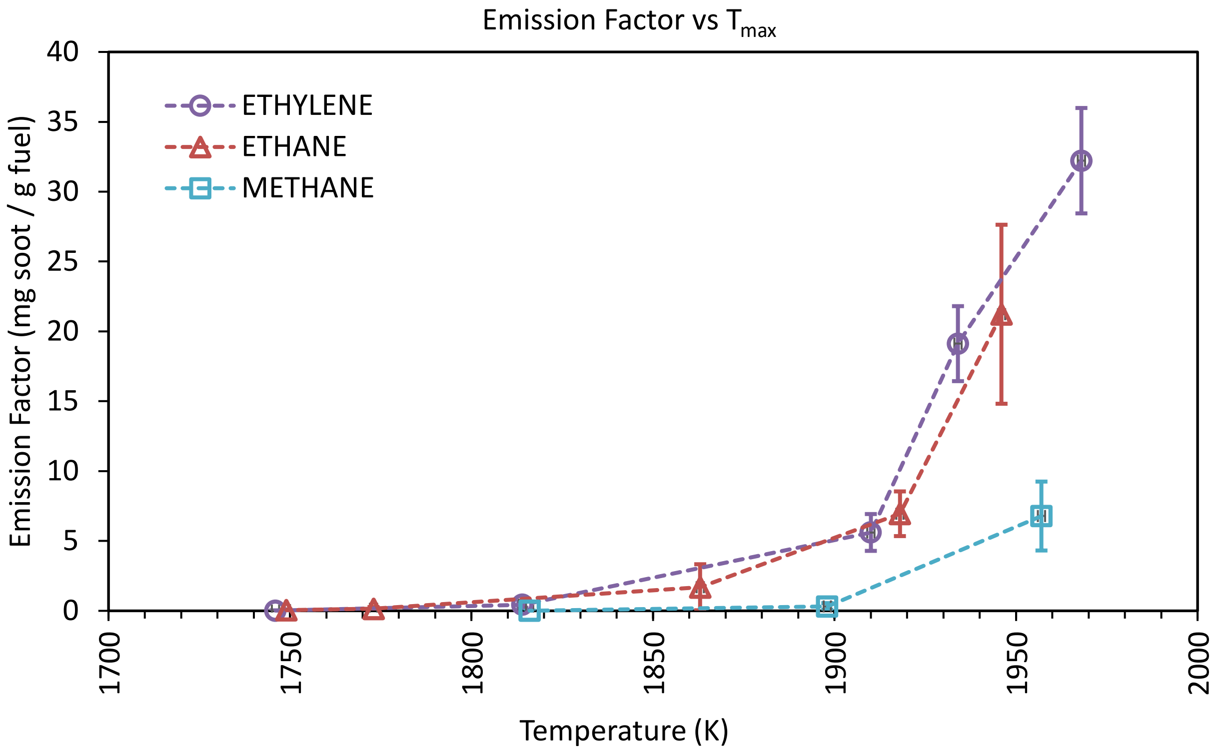

Figure 3.3. Emission factor compared with T_{max}. Emission data is consistent with a qualitative ranking of soot incandescence: ethylene > ethane > methane. Error bars represent the standard deviation of multiple measurements (2 to 12 data points depending on condition).

Investigation of upright flames indicates that the relative effect of temperature on soot volume yields is less than that of dilution [32]. The authors suggest that higher temperatures affect the upright co-flow flame by simultaneously increasing soot formation by pyrolysis and burnout by oxidization. For the purpose identifying tendency to soot, soot emission factor is similar to soot volume fraction (the spatial concentration of soot in flames primarily measured by optical methods). Particle oxidation will affect soot emission measurements differently than soot volume fraction. Soot particle residence time is extended in an inverted flame due to buoyancy [16]; therefore, it can be inferred that the particle growth period is longer and soot emissions of an inverted flame may be greater than a comparable upright flame.

3.1.2 *Emission Factor and Dilution Ratio*

Figure 3.4 plots soot emission factor against dilution ratio. Emission factor shows an inversely proportional correlation with dilution for all three fuels.

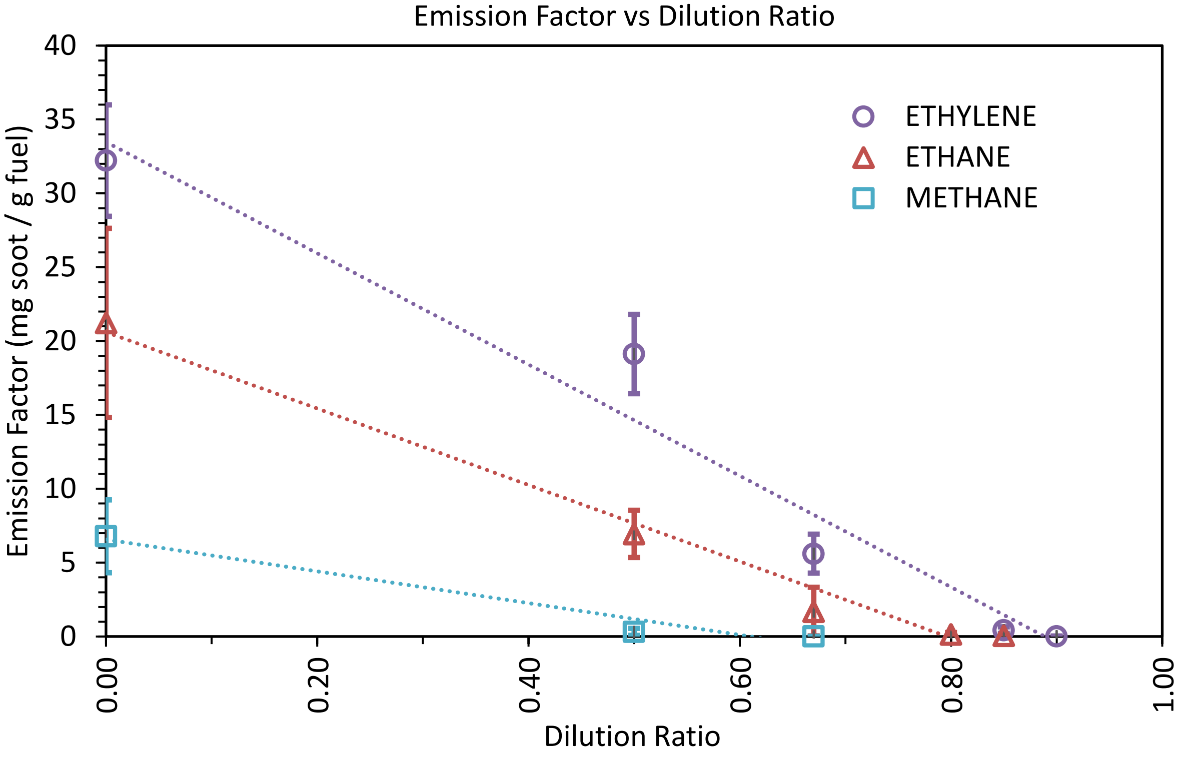

Figure 3.4. Emission factor compared with dilution.

The relative tendency to the soot of the fuels is apparent in Figure 3.4 (ethylene > ethane > methane) and is consistent with the literature [5]. Regardless of fuel type, argon introduction to the fuel stream (*i*) increases convective flow velocity, (*ii*) reduces the laminar flame speed, (*iii*) retards soot formation, and (*iv*) alters bulk thermal properties. Temperature effects soot nucleation, growth, and oxidation, while inert dilution may have a direct effect on soot emissions by reducing concentration of reactive species. The existing literature on diffusion flames examines the effects of dilution in co-flow and counterflow burners [7, 10, 11, 32]. The authors of reference [32] show dilution has a greater effect on tendency to soot than temperature. The cited work uses soot volume fraction as a metric for tendency to soot. In the IGFR, it is challenging to separate the thermally influenced soot formation rate (i.e. pyrolysis) from the particle burnout rate (i.e. oxidation) because soot emission factor is an ex-situ measurement. The conclusion that the effect of dilution on tendency to soot is relatively greater than the effect of temperature is a supported finding.

3.1.3 *Carbon Conversion Factor*

Carbon conversion factor (CCF) is an alternative soot yield metric. CCF is defined as the grams of carbon in fuel converted to milligrams of soot. For reference, carbon mass flow rates of ethane, ethylene, and methane for the flame conditions in this work are 0.1208 g/min, 0.1205 g/min, and 0.1190 g/min, respectively. Carbon mass flow rates are constant within 0.002 g/min. For comparison, fuel mass flow rates are constant within 0.1 g/min. Results are similar to emission factor and further analysis is not explored.

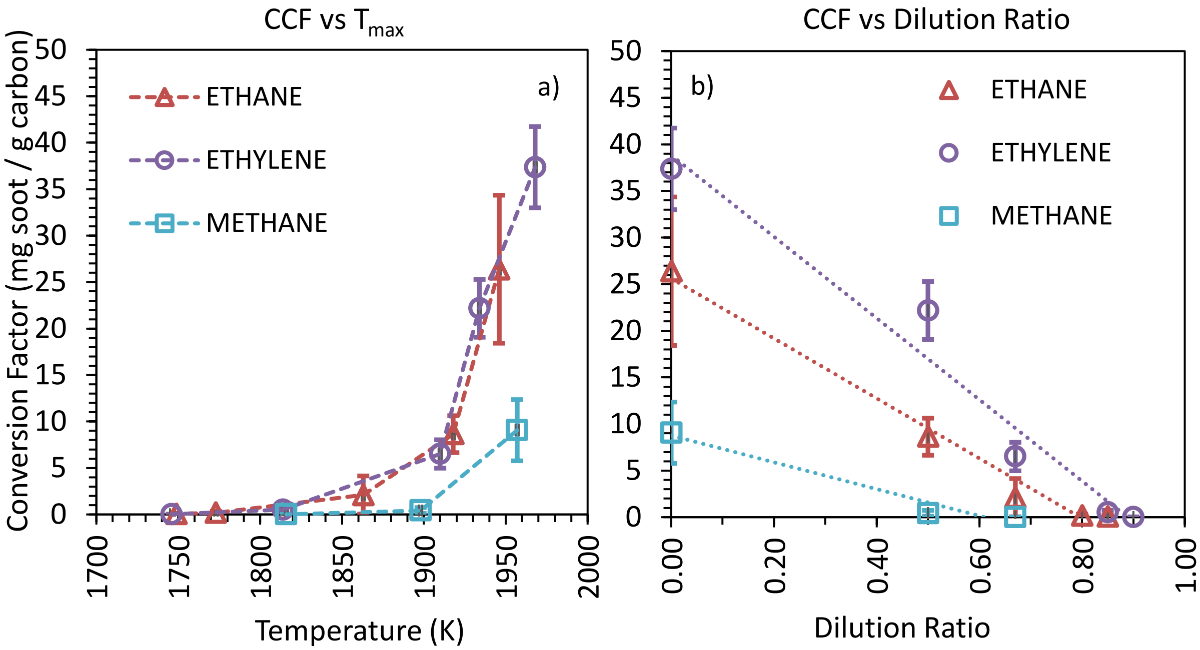

Figure 3.5. Carbon conversion factor results. CCF compared with T_{max} (a) and dilution ratio (b).

3.1.4 *Organic Carbon*

Figure 3.6 summarizes results from organic carbon (OC) measurements. The organic carbon fraction (OC/TC) in soot emissions increases with dilution ratio and decreases with temperature.

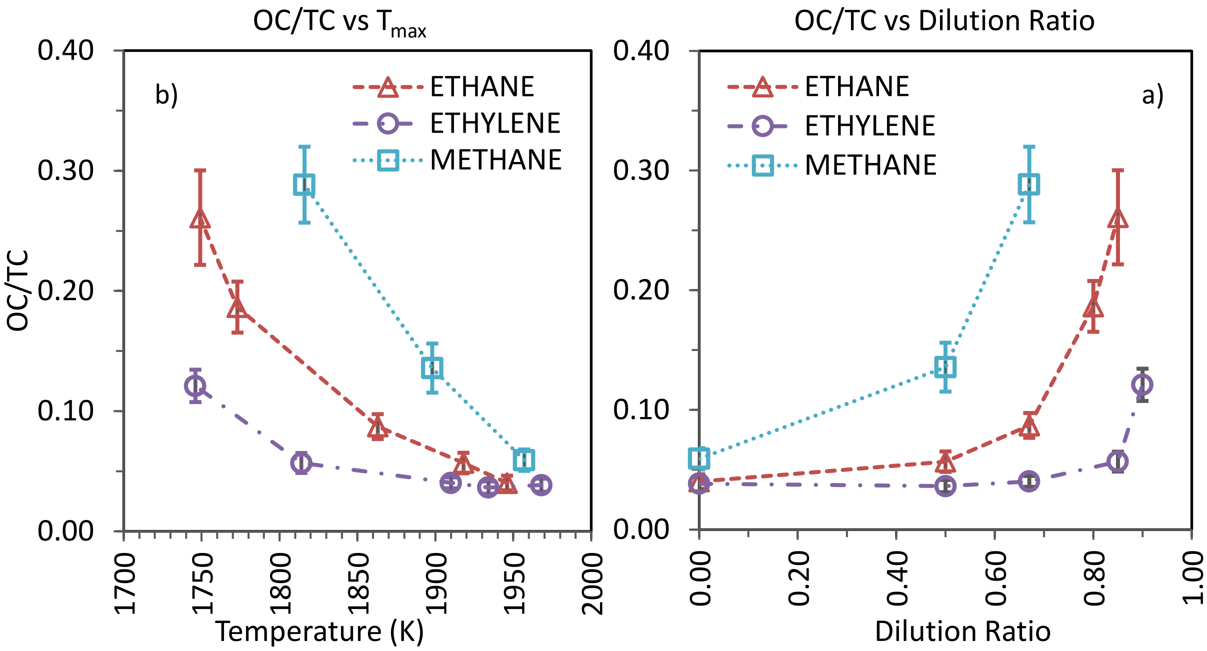

Figure 3.6. Organic carbon results. OC/TC vs dilution ratio (a) and vs T_{max} (b). High dilution and low temperature are correlated with a higher fraction of organic carbon in soot emissions. Error bars represent reported uncertainty associated with OC and EC measurement.

The physicochemical processes involved in soot formation are complex. A key first step in soot formation is fuel pyrolysis, the thermal process responsible for converting the hydrocarbon fuel into soot precursors, i.e. PAHs (polyaromatic hydrocarbons). Diffusion flames benefit from the lack of oxidative attack during the pyrolysis phase of soot formation [5]. Lower flame temperature can result in a higher concentration of organic carbon in soot by limiting pyrolysis. Conversely, high-temperature conditions result in more complete conversion of fuel to black carbon.

As shown in the emission factor results, high temperatures (low dilutions) are correlated with increased soot emissions. Practical high dilution combustion systems can be susceptible to extinction when nearing lower limits (e.g. lower temperature limit). A combination of the preheat of reagents and dilution has potential to lower soot emissions and increase thermal efficiency.

3.1.5 *Preheat*

The preheat temperature measurements and emission data shed insight into the soot formation in the IGFR (Figure 3.7). For an inlet temperature increase of 200 K, flame temperatures increase between 100-150 K (e.g., 174 K for ethylene 0.90 dilution). Temperature measurement and adiabatic calculations show similar increases, e.g., for 200 degrees preheat for ethane 85% dilution, the measured ΔT_{max} = 125 K and calculated ΔT_{ad} = 124.7 K.

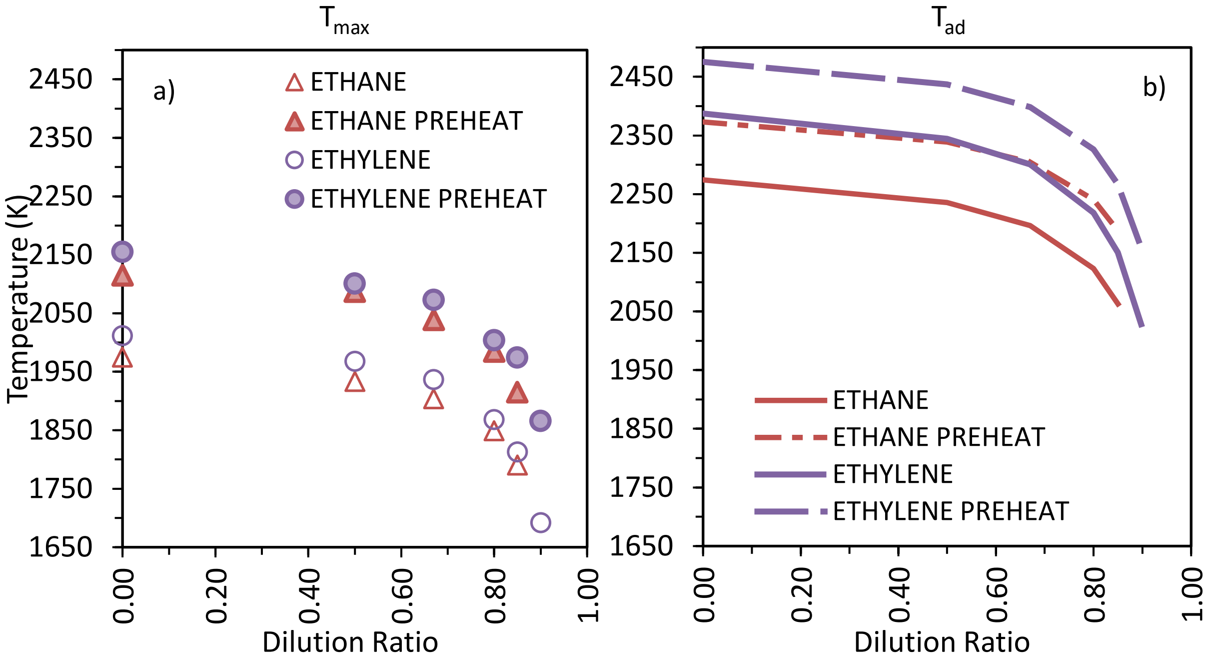

Figure 3.7. Preheat condition temperature results. Measured maximum temperatures (a) are presented next to adiabatic equilibrium temperatures (b) for comparison.

Increasing initial temperature of reagents raises the enthalpy within the system, increasing reaction rates and laminar flame speed. Increasing temperature results in soot emissions increase.

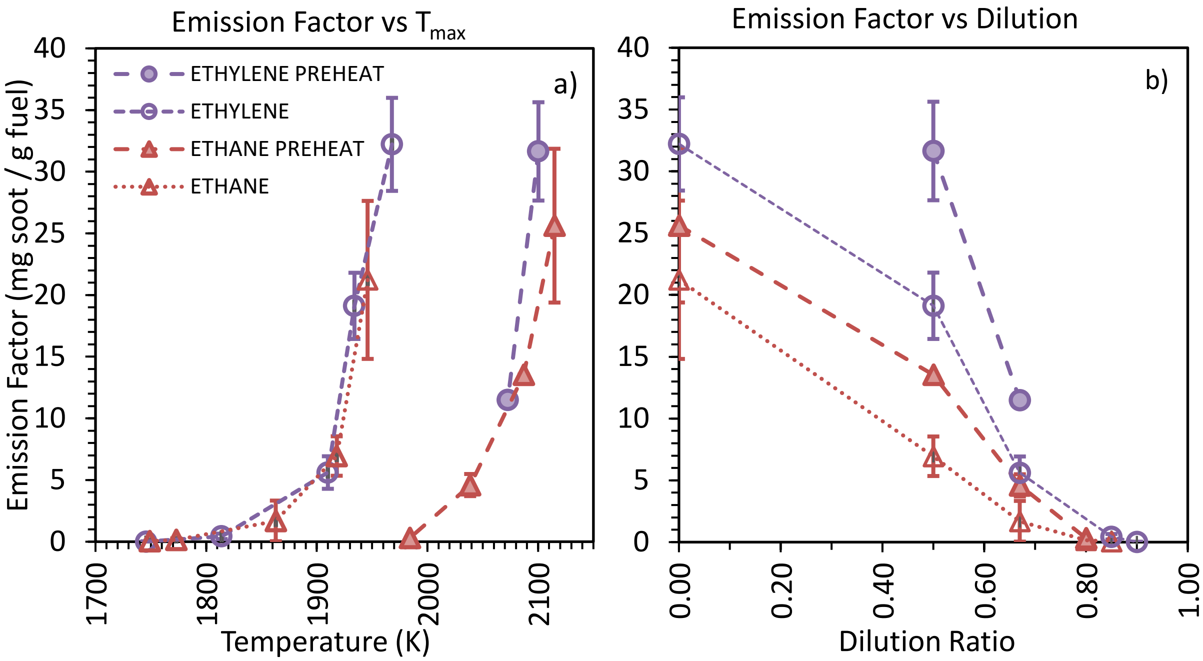

Figure 3.8. Preheat conditions and emission factor. Comparison of emission factor with T_{max} (a). Comparison of dilution with soot emission factor (b). Plot (b) uses the same legend as (a). Preheat result for ethylene is limited due to poor filter mass stability.

Comparison of ethane preheat and non-preheat emission factors vs. T_{max} does not show significantly higher soot emissions at higher preheat temperatures. At equivalent dilutions, an increase in preheat shows increased soot emission factor. These results support the previous discussion related to the relative role of dilution on a flames' tendency to soot (Figure 3.4. Emission factor compared with dilution.). Our limited preheat results, show consistent soot emission trends; however, there is some uncertainty in the emission factor measurements due to filter stability.

Ethane and ethylene preheat conditions were characterized with the intent of separating the effect of dilution and temperature on OC/TC. For the preheat soot samples collected in this study, carbon measurements were not performed as a majority of soot samples did not meet the concentration requirement of 5 to 400 micrograms per square cm for accurate results.

3.2 PEAK-LUMINOSITY REGION TEMPERATURE

Peak-luminosity temperature, T_s*, is proposed as a soot temperature measurement at peak red-spectrum luminosity. The determination of T_s* is motivated, by (*i*) the difference between maximum temperature and temperature in the soot maturation region and (*ii*) the lack of a spatially (i.e. radially) resolved temperatures for IGFR conditions.

3.2.1 *Dilution Ratio*

Figure 3.9 shows T_s* results compared with dilution. Ethane and ethylene show similar trends as T_{max}, while methane has an unexpected upward trend with increasing dilution.

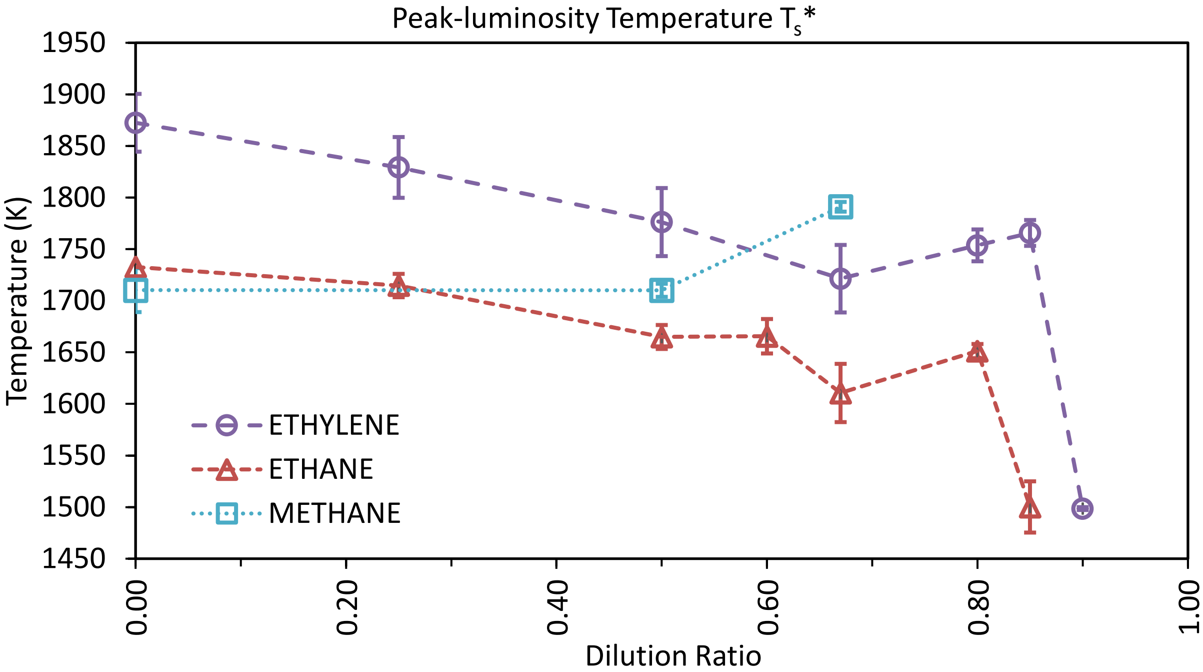

Figure 3.9. Peak-luminosity temperature results. T_s* decreases with dilution ratio for ethane and ethylene. Methane T_s* increases with dilution. Error bars represent standard deviation.

The jump in T_s* at high dilutions (e.g. 0.80) is inconsistent with T_{max}. To ensure outliers were not a result of poorly imaged conditions, three sets of flame images were taken with varying exposure (two sets for methane) and the results were averaged. Possible measurement error and the effect of the flame structure were considered to explain the unusual temperature trends.

3.2.2 *Comparison with Maximum Temperature*

Evaluation of a method for determining T_s* and the suitability of T_s* as a soot-temperature metric is one of the goals of this work. A direct comparison between T_s* and T_{max} shows mixed results.

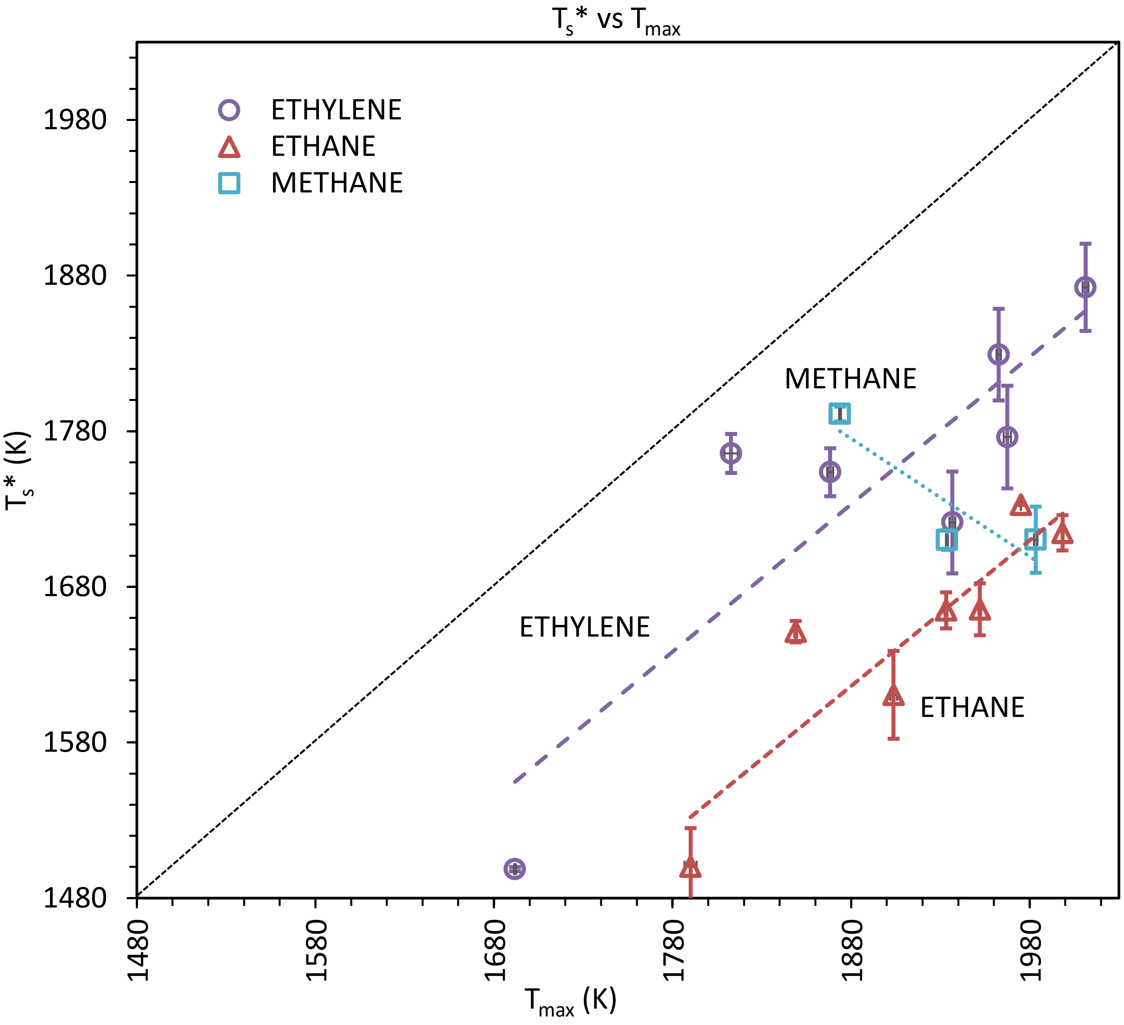

Figure 3.10. T_s* compared with T_{max}. Ethane and ethylene show similar positive correlations. Methane shows a negative correlation.

3.2.3 *Data Outliers*

The unusual increase in T_s* at high dilutions provides insight into the inverted flame structure (Figure 3.11). Differences in the structure are observed between fuels (i.e. ethylene is a shorter flame with a larger diameter when compared to ethane (Figure A.1, Figure A.2). However, all fuels exhibit similar axial temperature gradient trends with increasing dilution.

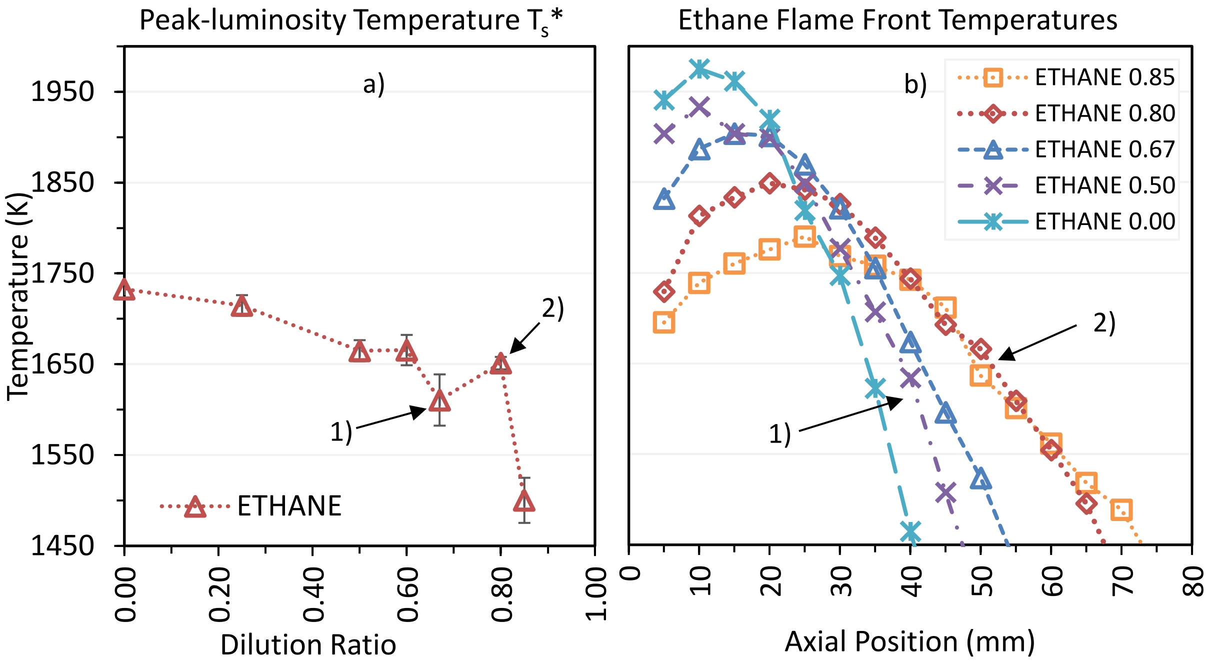

Figure 3.11. Ethane T_s* outlier and flame front profile. Ethane 0.67 dilution case is indicated by points (1a) and (1b). The axial position for the max temperature of ethane 0.80 dilution case is shifted downstream as indicated by points (2a) and (2b). Temperature gradients of higher dilutions are lower and a higher T_s* temperature is determined for ethane 0.85.

The combined effects of dilution, soot radiation, and temperature on flame structure are complex. For all fuels, the axial flame front temperature gradients decrease with increasing dilution (Figure A.7-Figure A.10). As dilution increases, the location of maximum luminosity shifts downstream (Figure A.2, Figure A.3). For ethane, a transition occurs between 20 and 40 mm. A flame with a higher soot volume fraction will emit greater thermal radiation, thereby lowering flame temperature and contributing steeper temperature gradients at the lowest dilutions (e.g. ethane 0 to 0.67). Note that, the maximum soot volume fraction is not equal to maximum soot luminosity intensity because of the 4th-order temperature dependence of thermal radiation. Flame luminosity gives a relative estimation of soot concentration within a flame.

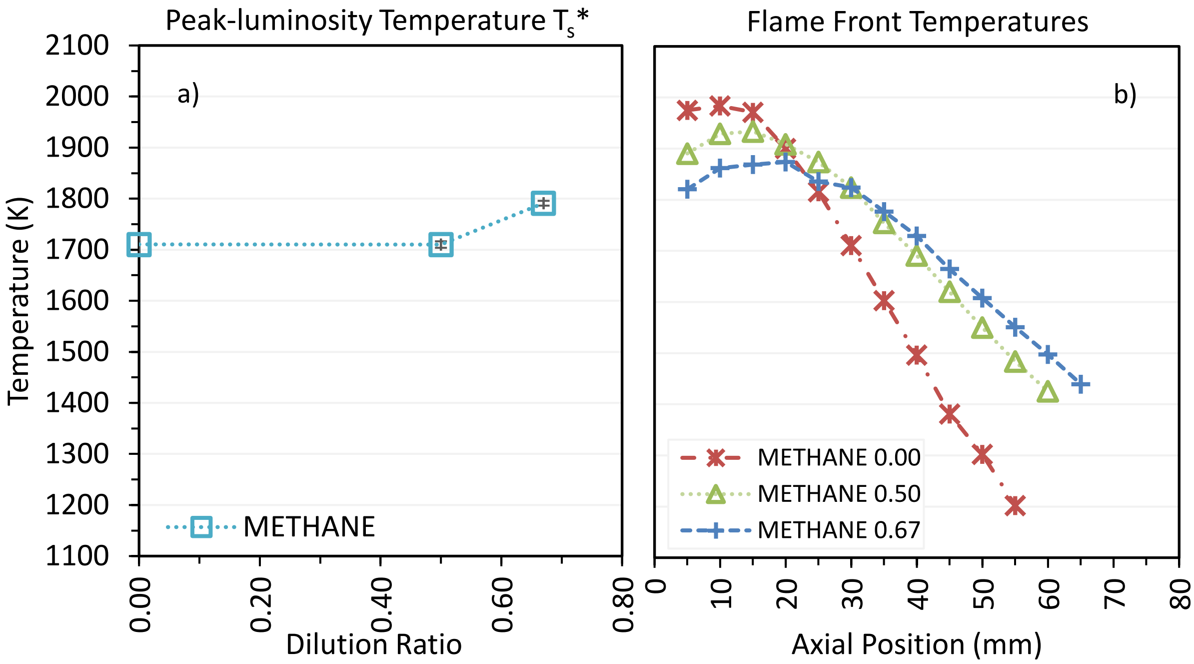

Figure 3.12. Methane T_s* compared with methane flame front profiles

Similar to ethane and ethylene, methane flame front gradients shift with dilution, i.e., past 30 mm a lower dilution methane flame does not measure a lower temperature. This pattern holds true when normalized for flame height, a result of dilution effecting reaction rate. The heat loss due to soot radiation effects the behavior of the temperature profile. However, in the case of methane 0.67 dilution, peak luminosity is upstream (i.e. higher) in the flame than methane 0.50 dilution. Soot volume fraction in methane 0.67 is known to be less, and soot incandescence is only visible with a relatively long exposure (Figure 3.13).

Methane Flame Images

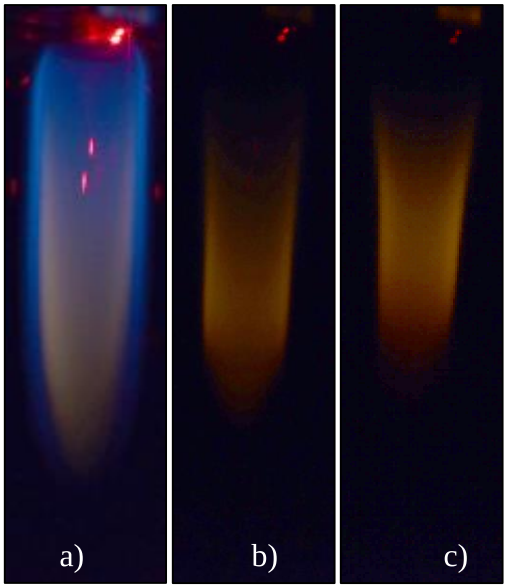

Figure 3.13. Images of methane flames. Flame images show 0.67 (a), 0.50 (b), and 0.00 (c) dilutions, i.e. high to low dilution.

Distinct color regions are visible in methane 0.67 dilution, typical for high-dilution conditions of all fuels. The chemiluminescence of radicals, seen in methane 0.67, is indicative of the flame front boundary [5, 34]. Soot inception location visibly progresses downstream with dilution. The temperature dependence of soot irradiance is more pronounced at lower concentrations, i.e., luminosity is an imperfect estimator of soot volume fraction. When compared to ethane and ethylene at highest dilutions, a greater radial distance between the flame front and visible soot region appears in methane flames.

The determined values of T_s* accurately identify flame front temperatures in the specified region. The discrepancy in soot volume fraction, radial structure, and temperature dependence lead to inconsistent results. Mitigating the high dilution outliers of T_s* is possible through reporting a range of flame front temperatures coinciding with peak luminosity. The resulting metric will be more relevant to actual soot temperature than maximum temperature or adiabatic temperature.

Chapter 4. CONCLUSIONS

In this work, inverted co-flow flames from an inverted gravity flame reactor operated on ethylene, ethane, and methane were characterized. Temperature and soot yields were taken as a function of fuel type, fuel dilution by argon, and preheat of air and fuel streams. A soot temperature metric based on soot luminosity analysis was explored. Specific conclusions include:

1. The maximum flame temperature and soot emission factor decrease with increasing argon dilution. The decrease in soot emissions is not a purely thermal effect, rather the decrease is likely due to a combination of reduction in concentration in species concentration participating in soot formation and decrease in flame temperature. A lower concentration of soot in flame reduces radiative heat loss and lowers axial thermal gradients.
2. Organic carbon fraction increases with fuel dilution and reduction of flame temperature. The limited carbonization of hydrocarbons at lower flame temperatures is the likely reason for high organic carbon content of the soot particle matter.
3. Preheat of reagents increases flame temperature and soot emissions for all dilutions. The effect of dilution on soot emissions appears greater than the effect of preheating. Increasing the inlet temperature increases collision energy, improving flame stability at lower dilutions. These findings can be applied to developing systems with reduced overall soot emissions. *Minimizing soot emissions from diffusion flames can be achieved by high fuel dilution with added preheat for increased flame stability*.
4. A peak-luminosity flame temperature, T_s*, is examined as an alternative metric for soot formation/maturation analysis. Initial analysis shows challenges in generalizing the results for all fuels. Thresholding flame luminosity for high and low characteristic soot temperatures is more accurate.

This work forms foundational data on a wide range of inverted diffusion flames. Spatial measurements of combustion species for local properties and comparison to upright flames is desired. Spatial measurements of IGFR conditions require reactor modification. A Computational Fluid Dynamic modeling of the IGFR could provide reasonable local property estimation and be useful buoyancy-controlled soot formation simulation. Additional future work is considered:

1. Inverted flame characterization work based on chemical structure, i.e., preheat vs OC/TC, can isolate the chemical effects of inlet preheat. Current OC/TC analysis is sensitive to concentration of soot deposition on the filter.
2. Improvements to peak-luminosity region temperature determination are desired. A more quantitative approach to determine the axial location of maximum soot concentration may be possible. High and low pass filters on images can isolate wavelengths, and it may be possible to normalize temperature dependence. Similar work uses CCD sensors which provide higher quality image data. Inevitably, spatially resolved temperatures are necessary to gain a more accurate peak-luminosity temperature and resolve radial error. Optical measurements require modification of the IGFR to reduce error introduced by a curved wall surface.

BIBLIOGRAPHY

1. Bond, T.C., et al., *Bounding the Role of Black Carbon in the Climate System: A Scientific Assessment.* Journal of Geophysical Research. D. , 118:5380-5552, 2013. **118**(11).
2. Jacobson, M.Z., *Short-term effects of controlling fossil-fuel soot, biofuel soot and gases, and methane on climate, Arctic ice, and air pollution health.* Journal of Geophysical Research: Atmospheres, 2010. **115**(D14): p. n/a-n/a.
3. Boström, C.-E., et al., *Cancer Risk Assessment, Indicators, and Guidelines for Polycyclic Aromatic Hydrocarbons in the Ambient Air.* Environmental Health Perspectives, 2002. **110**: p. 451-488.
4. Hailemariam, Y., H.M. Amiri, and K. Nugent, *Acute respiratory symptoms following massive carbon black exposure.* Occupational medicine (Oxford, England), 2012. **62**(7): p. 578.
5. Glassman, I., *Combustion*. 4th ed. ed, ed. R.A. Yetter. 2008, Amsterdam ; Boston: Amsterdam ; Boston : Academic Press.
6. Warnatz, J., U. Maas, and R.W. Dibble, *Combustion*. 2006, Springer: Berlin ; Heidelberg ; New York.
7. Abhinavam Kailasanathan, R.K., et al., *Effect of diluents on soot precursor formation and temperature in ethylene laminar diffusion flames.* Combustion and Flame, 2012. **160**(3).
8. Apicella, B., et al., *The Effect of Temperature on Soot Properties in Premixed Ethylene Flames.* Combustion Science and Technology, 2019: p. 1-13.
9. Glassman, I., *Soot formation in combustion processes.* Symposium (International) on Combustion, 1989. **22**(1): p. 295-311.
10. Glassman, I., *Sooting laminar diffusion flames: Effect of dilution, additives, pressure, and microgravity.* Symposium (International) on Combustion, 1998. **27**(1): p. 1589-1596.
11. Gulder, O.L. and D.R. Snellin, *Influence of nitrogen dilution and flame temperature on soot formation in diffusion flames.* Combustion and Flame, 1993. **92**(1-2).
12. Jerez, A., et al., *Measurements and modeling of PAH soot precursors in coflow ethylene/air laminar diffusion flames.* Fuel, 2019. **236**: p. 452-460.
13. Karataş, A.E. and Ö.L. Gülder, *Dependence of sooting characteristics and temperature field of co-flow laminar pure and nitrogen-diluted ethylene–air diffusion flames on pressure.* Combustion and Flame, 2015. **162**(4): p. 1566-1574.
14. Kholghy, M.R., et al., *Comparison of multiple diagnostic techniques to study soot formation and morphology in a diffusion flame.* Combustion and Flame, 2016. **176**: p. 567-583.
15. Snelling, D., et al., *Spectrally resolved measurement of flame radiation to determine soot temperature and concentration.* American Institute of Aeronautics and Astronautics. AIAA Journal, 2002. **40**(9): p. 1789-1795.
16. Stipe, C.B., *Inverted co-flow diffusion flame for producing soot.* Review of scientific instruments, 2005. **76**(2).
17. Davis, J., K. Tiwari, and I. Novosselov, *Soot morphology and nanostructure in complex flame flow patterns via secondary particle surface growth.* Fuel, 2019. **245**: p. 447-457.
18. Kazemimanesh, M., et al., *A novel miniature inverted-flame burner for the generation of soot nanoparticles.* Aerosol Science and Technology, 2019. **53**(2): p. 184-195.
19. Chakrabarty, R.K., et al., *Trapping and aerogelation of nanoparticles in negative gravity hydrocarbon flames.* Applied Physics Letters, 2014. **104**(24): p. 243103.

20. Mahamuni, G., et al., *Excitation-Emission Matrix Spectroscopy for Analysis of Chemical Composition of Combustion Generated Particulate Matter.* ChemRxiv. Preprint., 2019.
21. Birch, M.E. and R.A. Cary, *Elemental Carbon-Based Method for Monitoring Occupational Exposures to Particulate Diesel Exhaust.* Aerosol Science and Technology, 1996. **25**(3): p. 221-241.
22. *Sunset Laboratory Inc.*; Available from: http://www.sunlab.com/.
23. McEnally, C.S., et al., *Soot Volume Fraction and Temperature Measurements in Laminar Nonpremixed Flames Using Thermocouples.* Combustion and Flame, 1997. **109**(4): p. 701-720.
24. Hindasageri, V., R.P. Vedula, and S.V. Prabhu, *Thermocouple error correction for measuring the flame temperature with determination of emissivity and heat transfer coefficient.* Review of Scientific Instruments, 2013. **84**(2): p. 024902.
25. Lemaire, R. and S. Menanteau, *Assessment of radiation correction methods for bare bead thermocouples in a combustion environment.* International Journal of Thermal Sciences, 2017. **122**: p. 186-200.
26. Zhou, K., et al., *Validity evaluation on temperature correction methods by thermocouples with different bead diameters and application of corrected temperature.* International Journal of Thermal Sciences, 2018. **125**: p. 305-312.
27. Shaddix, C.R. *Correcting thermocouple measurements for radiation loss: A critical review*. in *National Heat Transfer Conference*. 1999. United States: American Society of Mechanical Engineers, New York, NY (US).
28. Hessel, R., et al., *Guidelines for Interpreting Soot Luminosity Imaging.* SAE International Journal of Engines, 2017. **10**(3): p. 1174-1192.
29. Li, Z., *Comparison of Laser-Extinction and Natural Luminosity Measurements for Soot Probing in Diesel Optical Engines*, Y. Gallo, et al., Editors. 2016, Warrendale, PA SAE International: Warrendale, PA.
30. Joo, H.I. and Ö.L. Gülder, *Soot formation and temperature field structure in co-flow laminar methane–air diffusion flames at pressures from 10 to 60 atm.* Proceedings of the Combustion Institute, 2009. **32**(1): p. 769-775.
31. Darrodi, M.M., et al., *A ground truth data set for Nikon camera's spectral sensitivity estimation*. 2014. p. 85-90.
32. Axelbaum, R.L. and C.K. Law, *Soot formation and inert addition in diffusion flames.* Symposium (International) on Combustion, 1991. **23**(1): p. 1517-1523.
33. Dandy, D. *Chemical Equilibrium Calculator with STANJAN*. 2019 [cited 2019; Checmical equilibrium calculator]. Available from: http://navier.engr.colostate.edu/code/code-4/index.html.
34. Peterson, K.A. and D.B. Oh, *High-sensitivity detection of CH radicals in flames by use of a diode-laser-based near-ultraviolet light source.* Optics letters, 1999. **24**(10): p. 667.
35. Santoro, R.J. and J.H. Miller, *Soot Particle Formation in Laminar Diffusion Flames.* Langmuir, 1987. **3**(2): p. 244-254.
36. Burke, S.P. and T.E.W. Schumann, *Diffusion flames.* Proceedings of the Symposium on Combustion, 1948. **1**(C): p. 2-11.

APPENDIX A: FLAME IMAGES

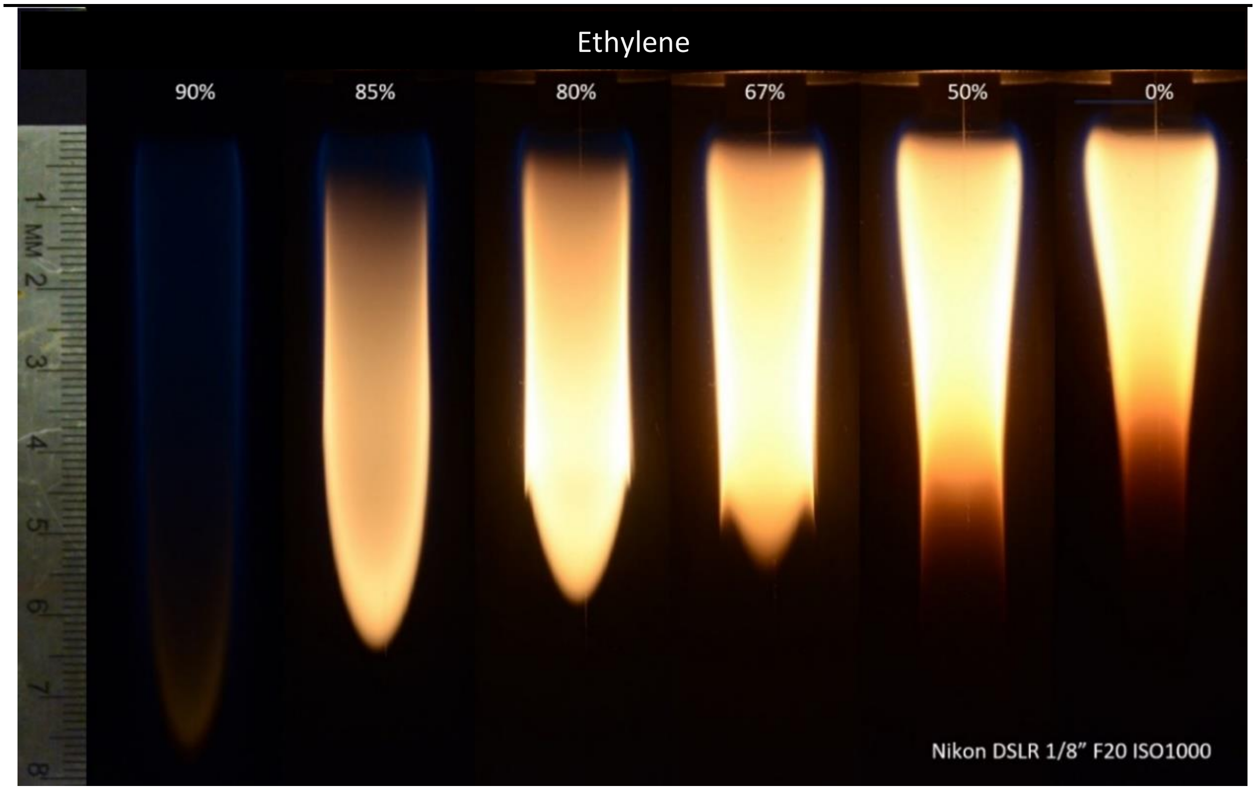

Figure A.1. Ethylene flame images. These images are not used in image analysis. Brightest regions in these images are overexposed making identification of peak luminosity region ambiguous. Images taken for T_s* were at lower exposure settings.

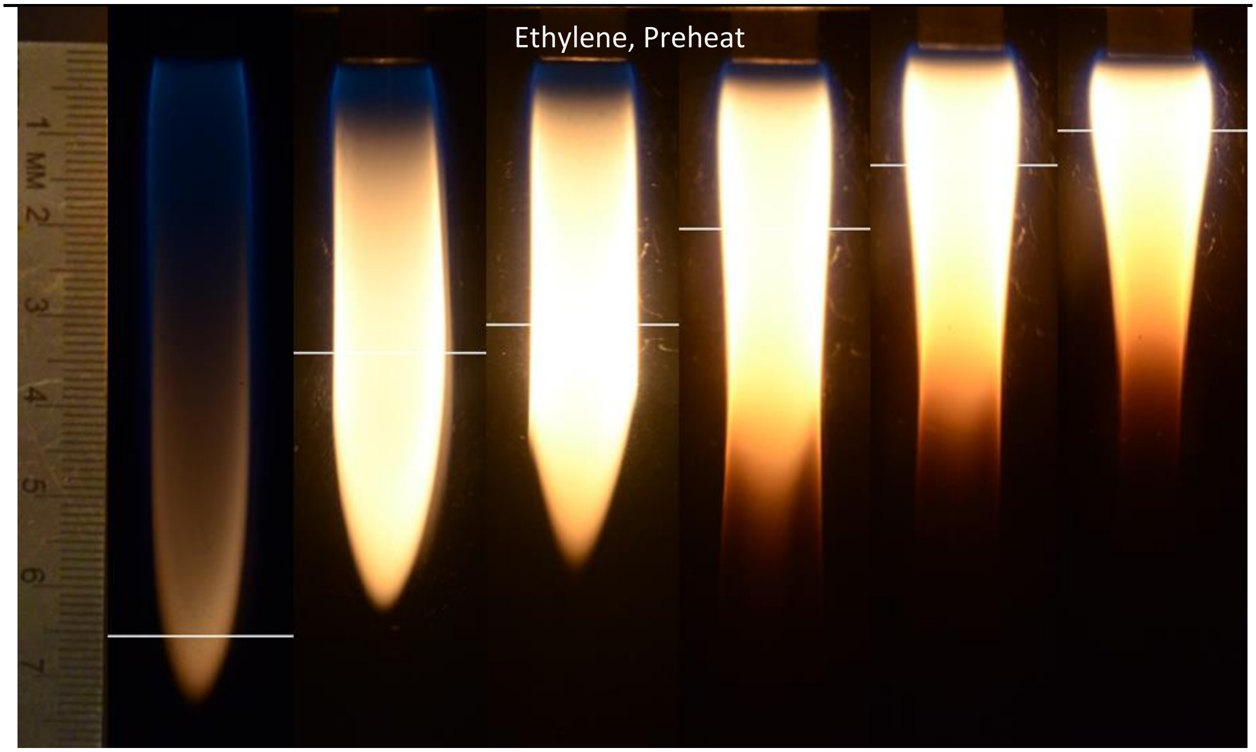

Figure A.2. Ethylene preheat flame images. Horizontal white lines are the median axial location of peak pixel luminosity. Position of luminosity moves downstream with dilution. The transition of winged flame to fully closed tip ethylene flame occurs between 0.67 and 0.90 dilution. Camera settings match Figure A.1. Overexposure is visible in the brightest regions of the flame.

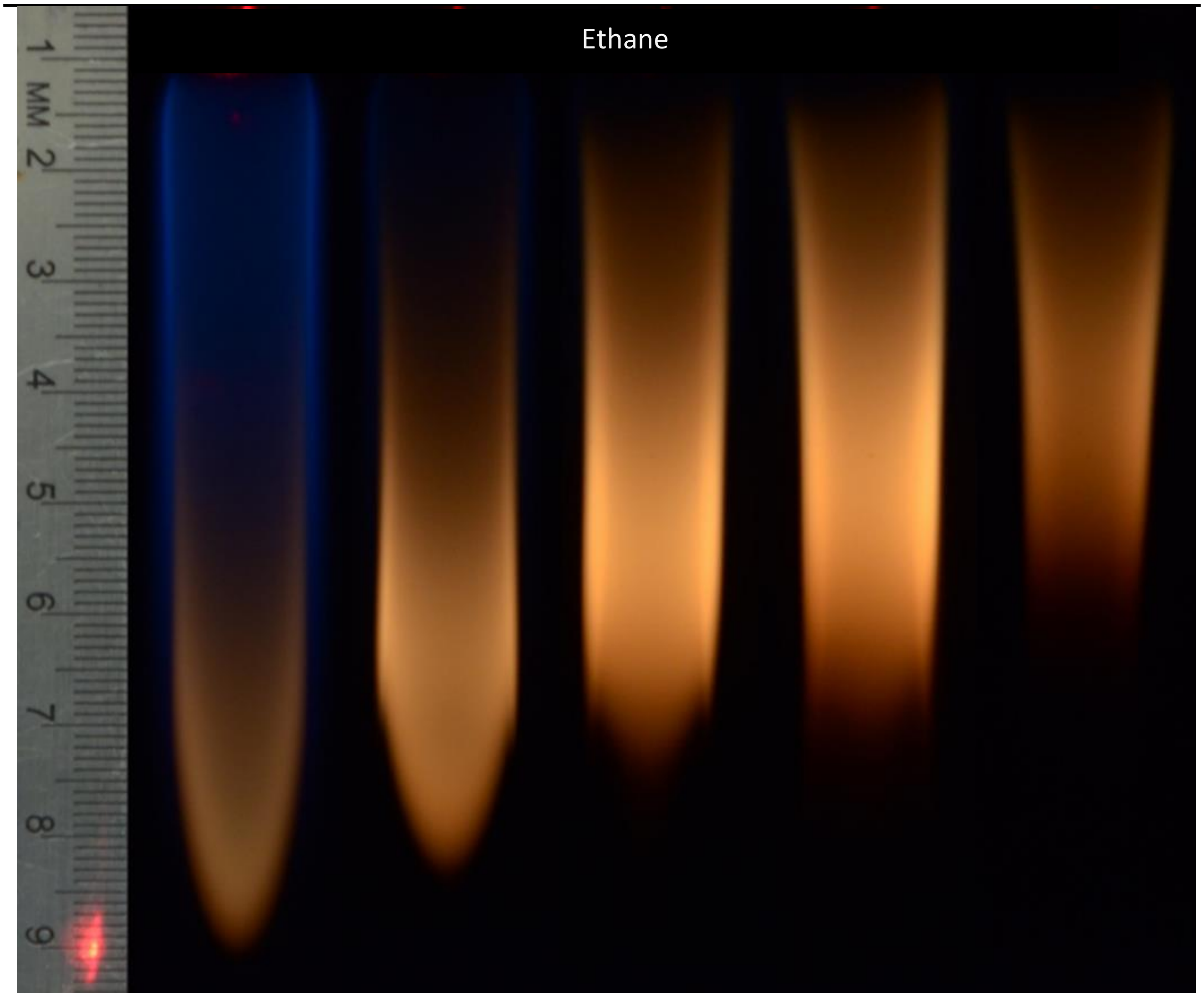

Figure A.3. Ethane flame images. Dilution ratios from left to right are 0.85, 0.80, 0.67, 0.50, 0.00. Images are at a lower exposure for more effective image analysis.

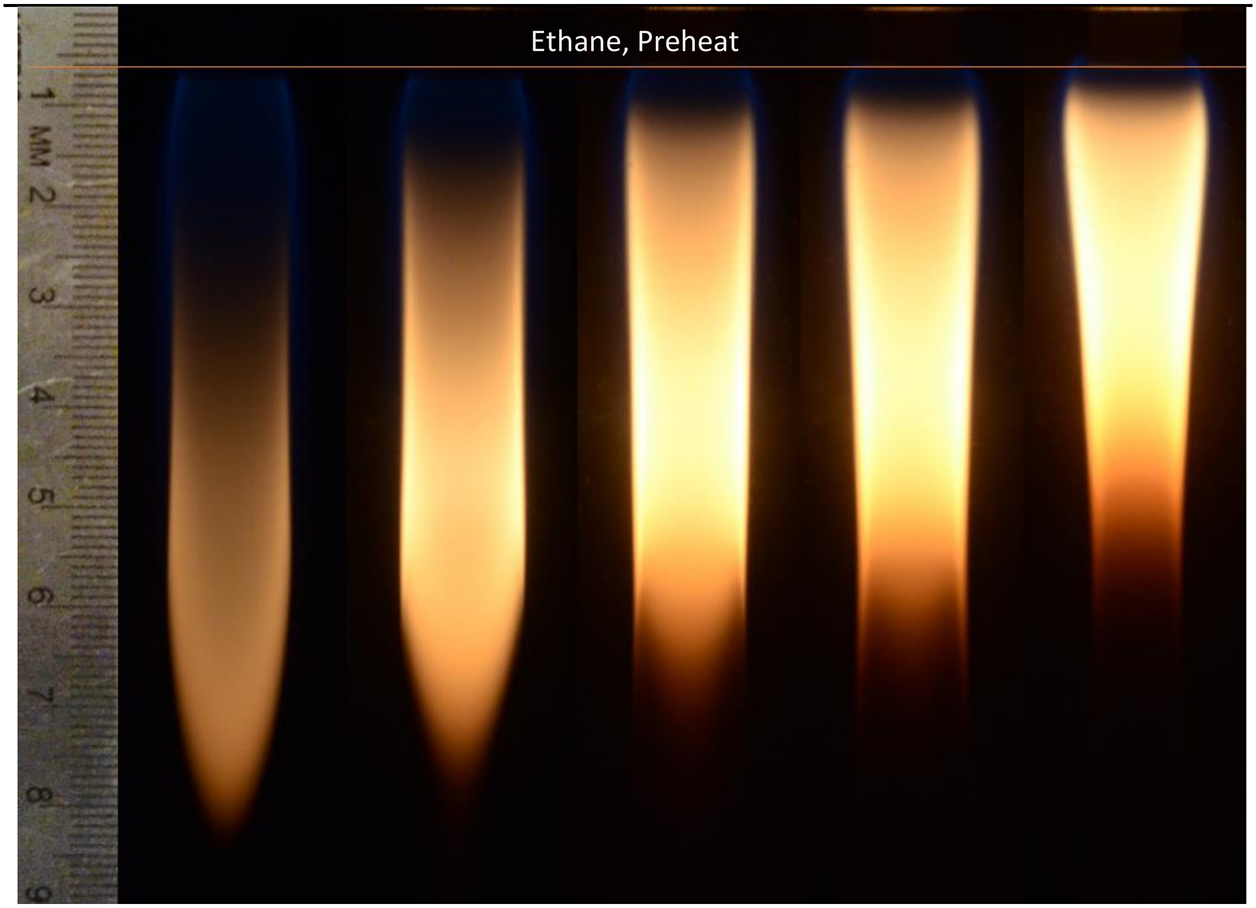

Figure A.4. Ethane preheat flame images. Same dilutions as non-preheat (Figure A.3). These images are included for structure and comparison and are not used in image analysis. Preheat has a visible effect on location of soot formation zone. Comparing 0.85 (left-most) with non-preheat (Figure A.3), initial luminosity appears 20 mm closer to fuel tube inlet, i.e., incandescing soot particles appear sooner in preheated flames.

APPENDIX B: IMAGE ANALYSIS

Image Spectral Layers

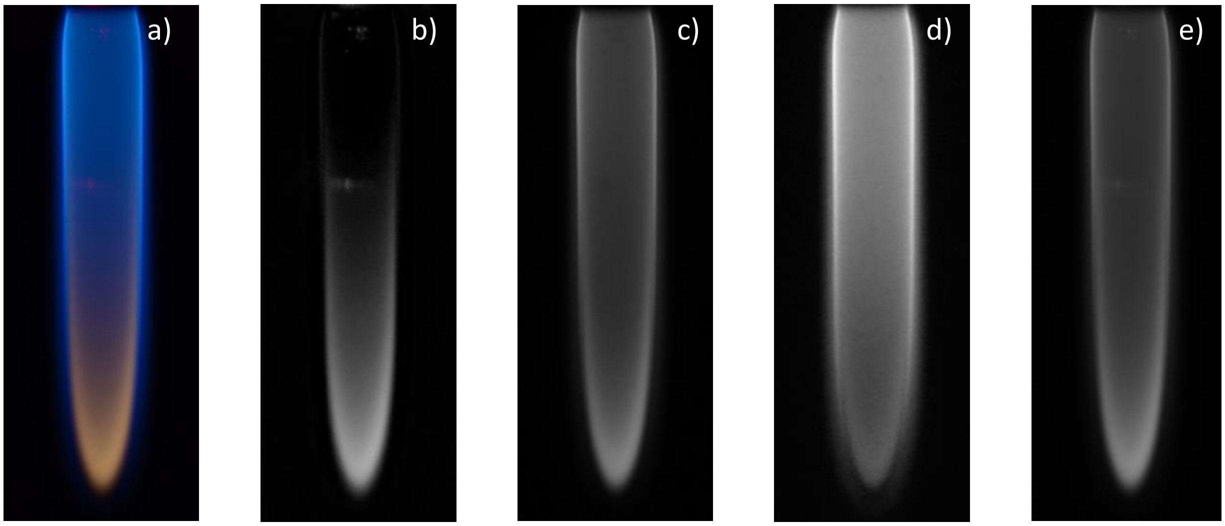

Figure A.5. Example RGB layers of jpg-file flame image. Left to right: red (b), green (c), blue (d) layers and MATLAB’s *rgb2gray* function (e) of initial image (a). Soot incandescence at tip (a) corresponds best with red layer (b). Chemiluminescence (a) matches with blue layer (d).

Spectral Response of Nikon D5100

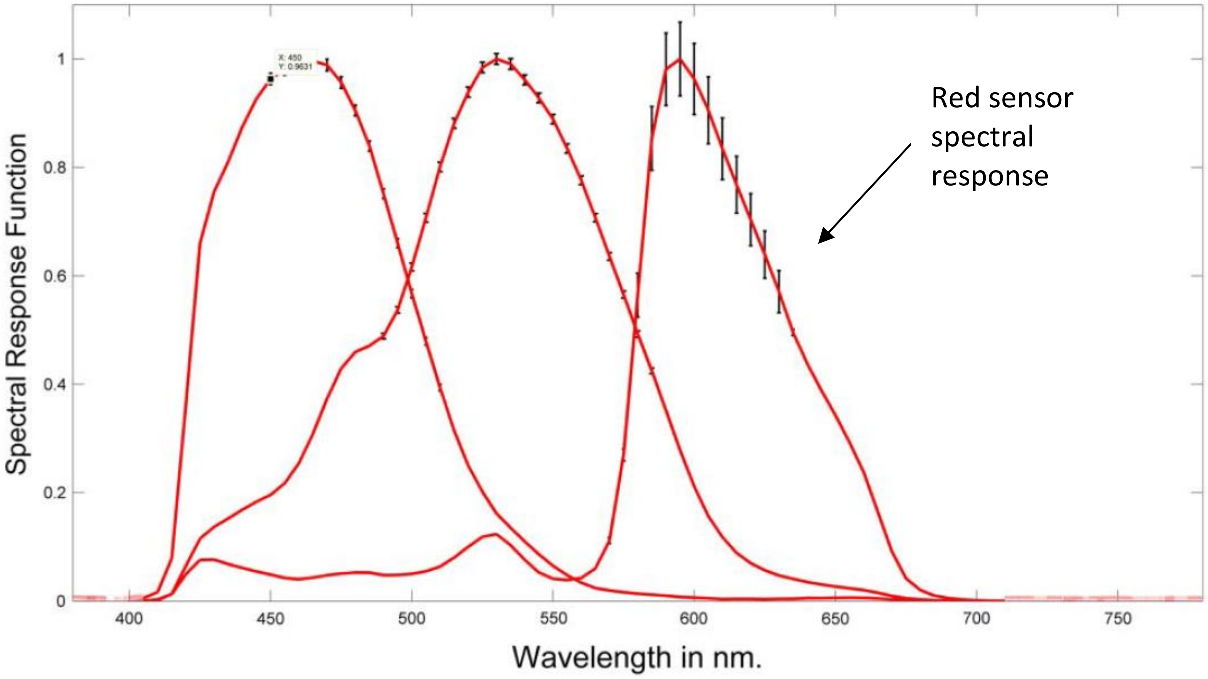

Figure A.6. Spectral sensitivity of Nikon D5100. Figure reproduced from reference [31]. Soot incandescence peaks in the infrared, therefore the red sensor (peak at 600 nm) will best capture soot radiation intensity.

APPENDIX C: FLAME FRONT TEMPERATURES

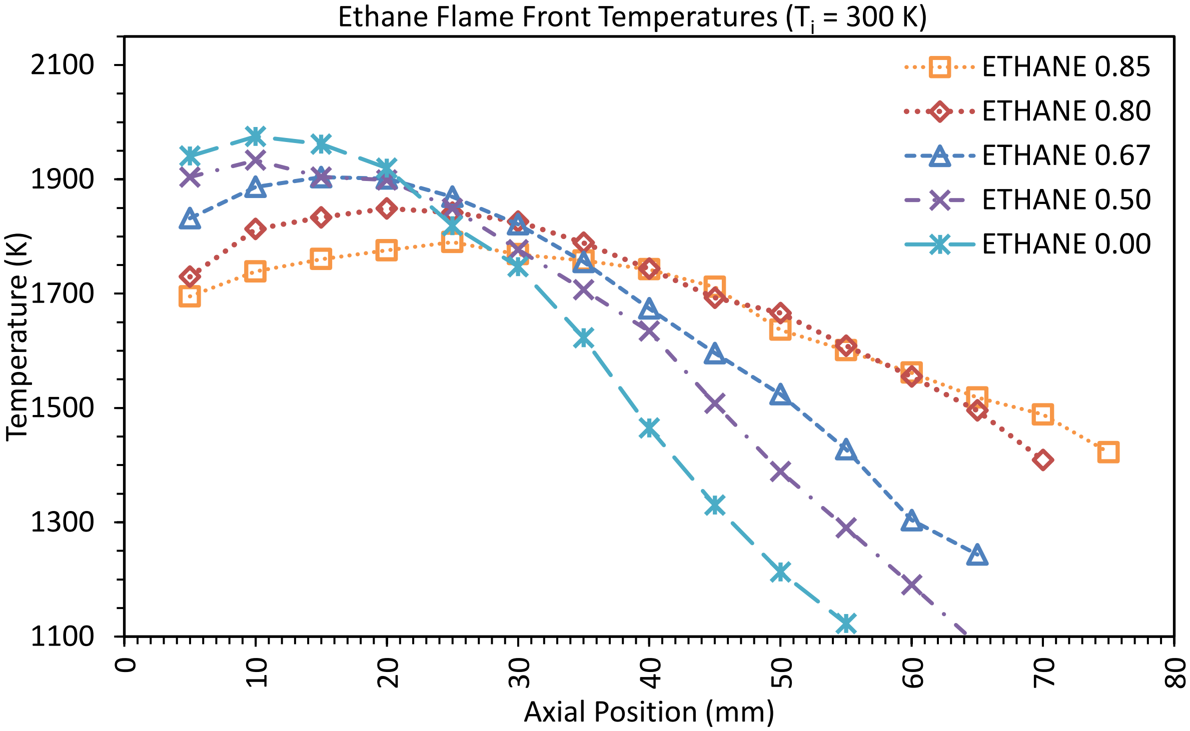

Figure A.7. Ethane flame front temperatures for non-preheat conditions

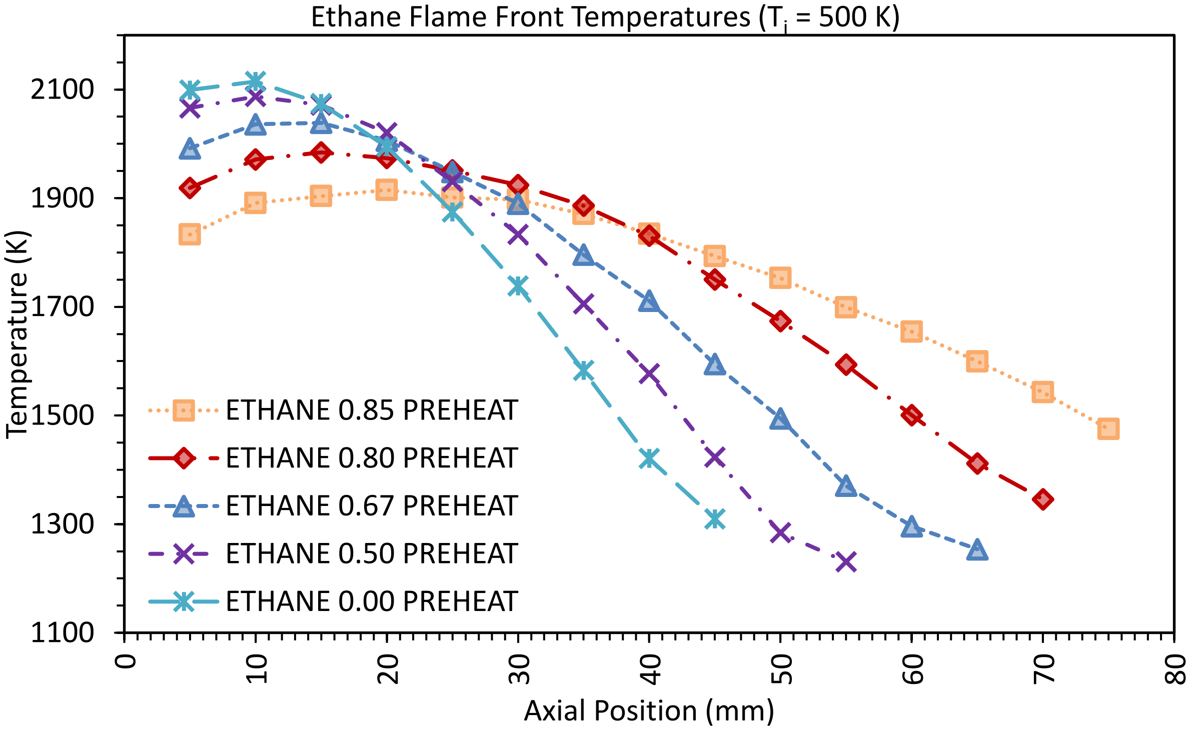

Figure A.8. Ethane flame front temperatures for preheat conditions.

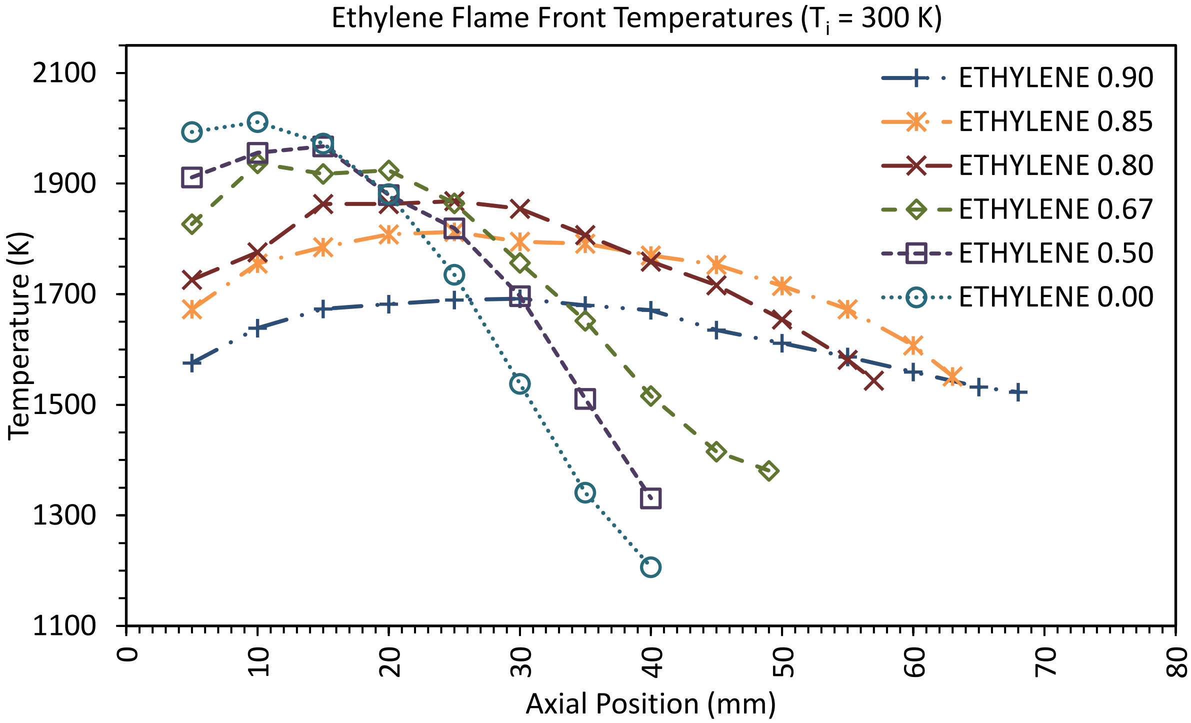

Figure A.9. Flame front profiles of ethylene at non-preheat conditions

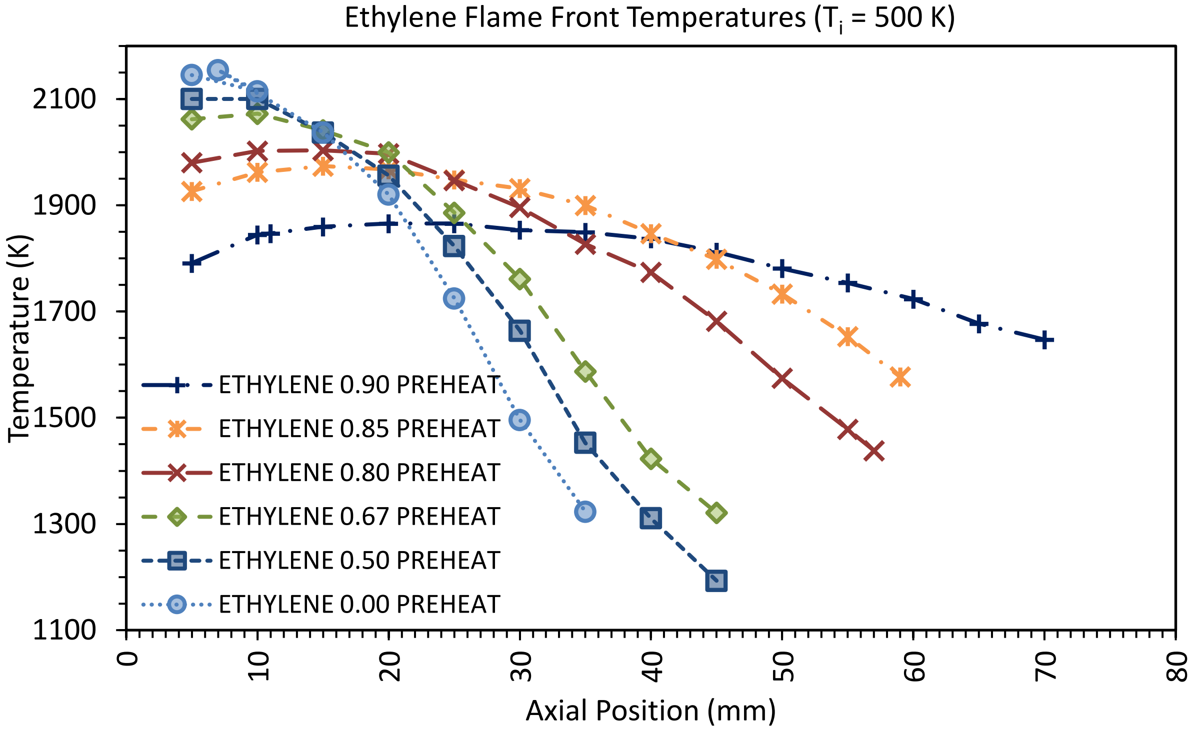

Figure A.10. Flame front profiles of ethylene at preheat conditions.

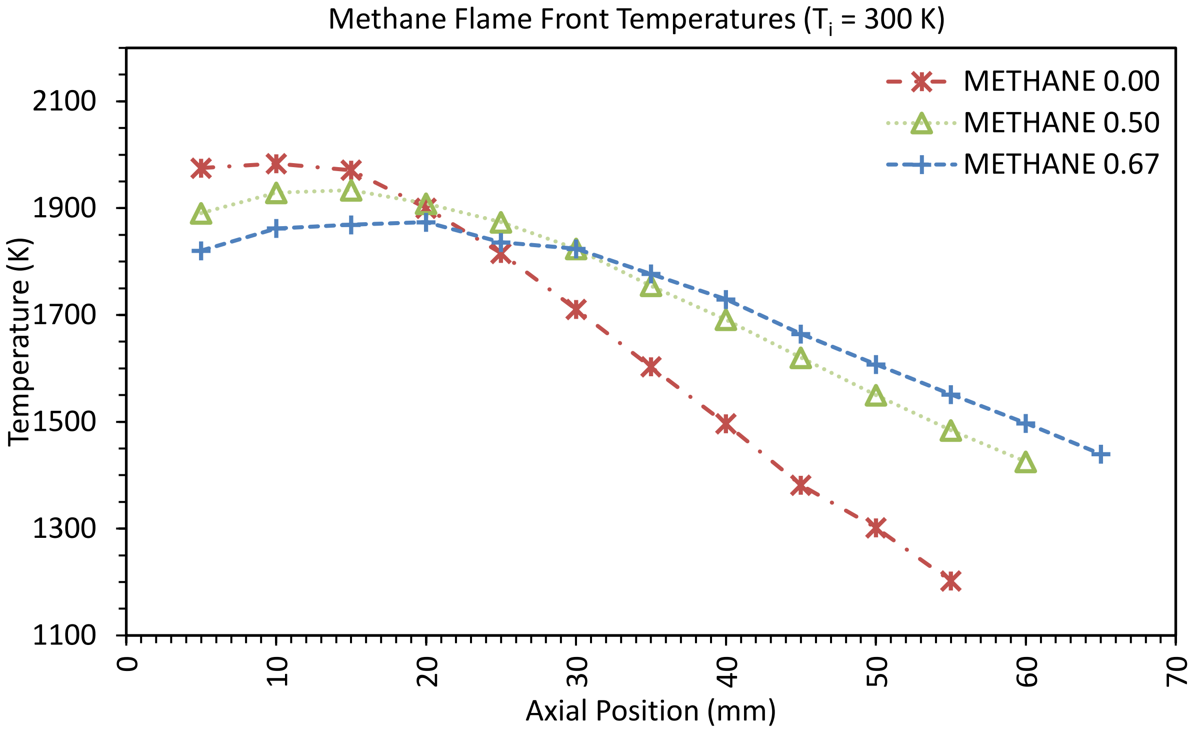

Figure A.11. Flame front profiles of methane conditions.

APPENDIX D: CO-FLOW DIFFUSION STRUCTURE

Observations of IGFR flame temperature field indicate overventilated inverted flames (Φ < 1) have gradients and structure similar to overventilated upflow co-flow flames [10, 12, 35]. Axial and radial temperature gradients in a laminar upflow co-flow diffusion flame have a predictable profile (Figure A.13). Radial temperature gradients are greatest near the fuel tube inlet and decrease with axial distance.

Overventilated vs Underventilated

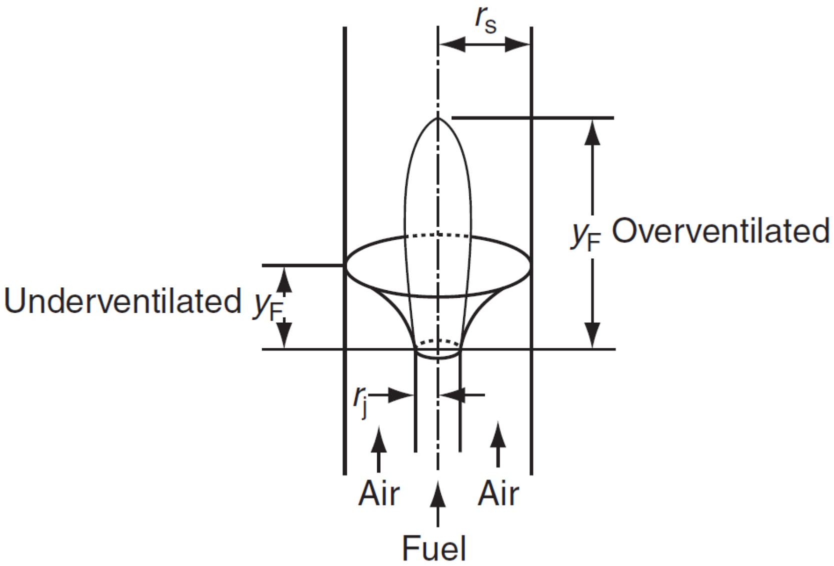

Figure A.12. Underventilated and overventilated co-flow diffusion flame regimes. Figure reproduced from reference [5].

Typical co-flow diffusion flames fall into two categories: overventilated (Φ < 1) and underventilated (Φ > 1). A classic example of an overventilated diffusion flame is a candle burning in open air, where buoyant forces drive heated gases into the elongated shape. The same candle in microgravity would take on a spherical shape due to absence of buoyant forces. IGFR conditions produces a unique overventilated shape due to the opposed buoyant forces. The pressure of the sheath air in the enclosed tube of the IGFR maintains the inverted shape. Upflow co-flow flames have a mathematical predictable shape (r_s,y_F) first proved by Burke and Schumann [36]. The predictive formula is not compared to inverted flames in this work.

Ethylene Upflow Co-flow Diffusion Flame

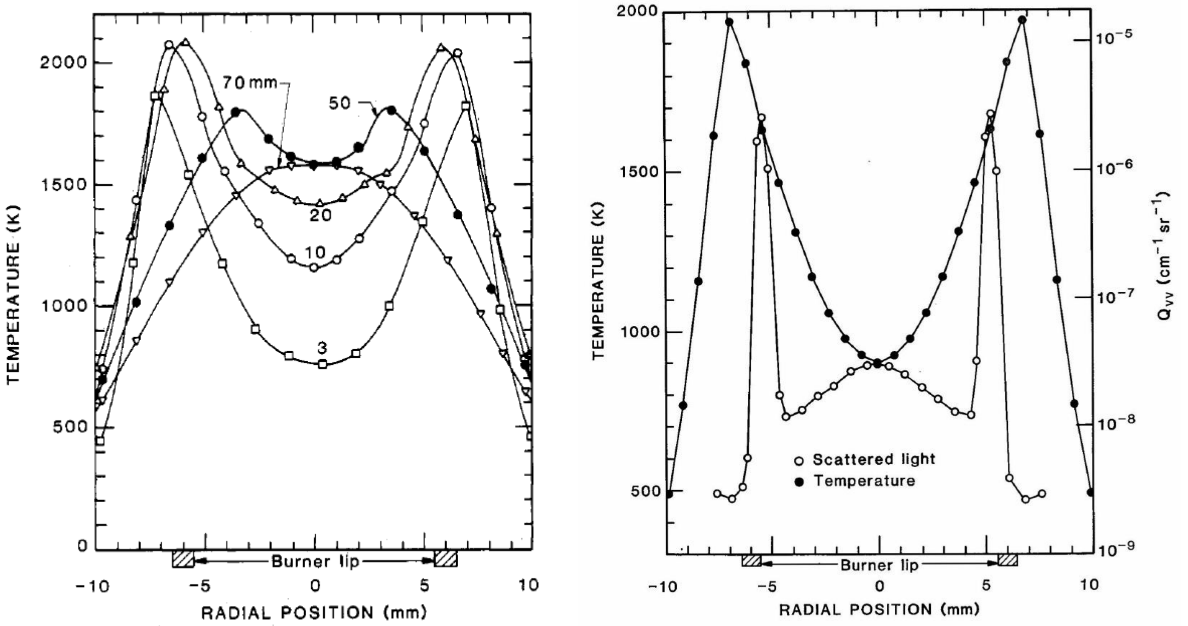

Figure A.13. Upflow co-flow ethylene flame from similar burner. Figures copied from reference [35]. Experimental fuel and air flow rates are 0.231 and 42.8 slpm respectively. Burner has fuel tube inner diameter of 11.1 mm and air tube outer diameter of 101.6 mm. Radial temperature gradient decrease with height (*left*) is expected to be similar to a comparable inverted flame. Scattered light measurements at 5 mm above burner show peak soot region 1.5 mm inside maximum temperature location (*right*). Near where radial gradients are largest (*z = 5 mm*), the difference between maximum temperature and temperature at maximum soot concentration is approximately 300 K.

APPENDIX E: MANIFOLD TEMPERATURES

Inlet manifold temperatures are measured during IGFR operation. A steady increase in temperature due to the radiant heating by the flame is observed (Figure A.14). Some error in presented temperature data is expected from the gradual flame-induced preheat (i.e. natural preheat).

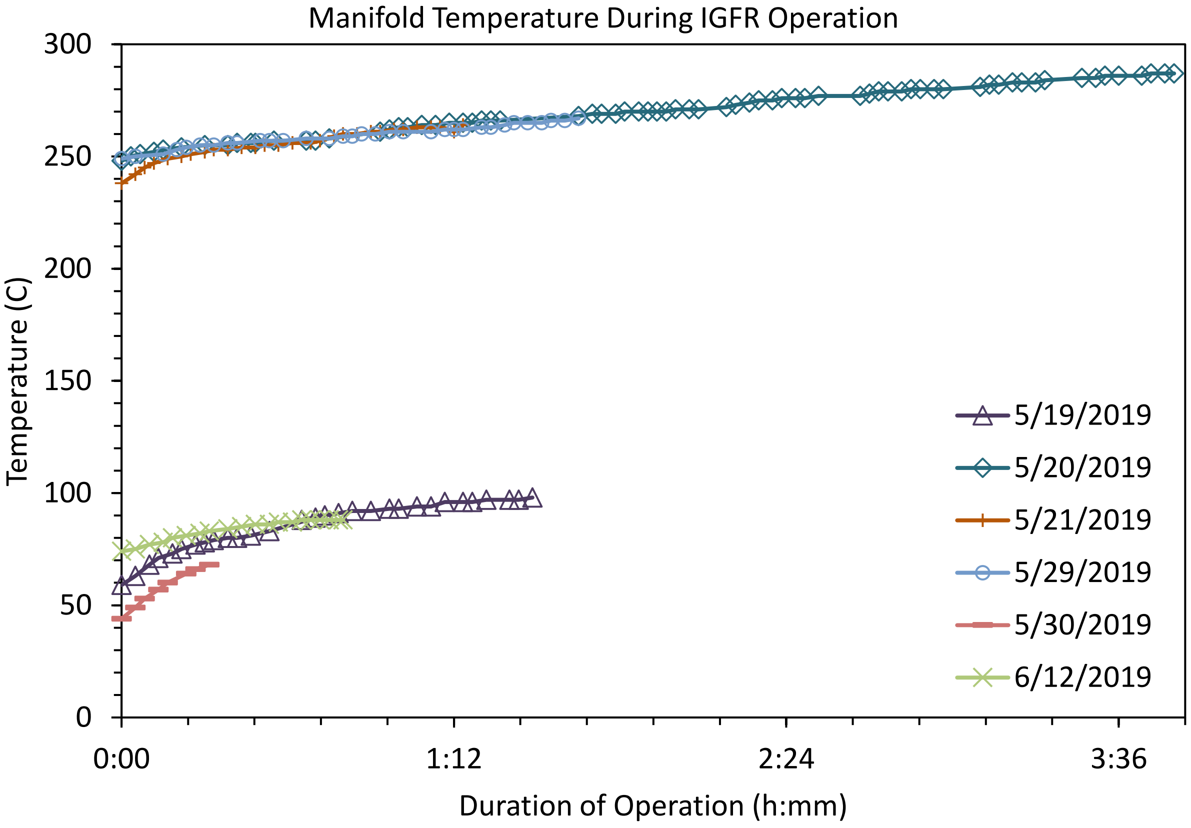

Figure A.14. Representative set of manifold temperatures during IGFR operation. Preheat conditions (*dates 5/20, 5/21, 5/29*) show steady increase with operation. Temperature increase is initially greater for non-preheat (*dates 5/19, 5/30, 6/12*), before leveling out. Measurement procedure calls for data collection 30 minutes after IGFR ignition to reduce the influence of operation preheat on inlet temperature.

APPENDIX F: NUSSELT NUMBER

An accurate Nusselt number is challenging to determine. Literature relies on both qualitative assessment of the junction geometry and quantitative correlations of the value [27]. Literature states that determining thermocouple junction geometry (spherical or cylindrical) can be quantitively determined with the Biot number (non-dimensional ratio of heat transfer resistances inside a body and at the surface of a body) and the bead-to-wire ratio. Generally, a bead-to-wire ratio above 3 indicates the junction is more aptly modeled as a sphere. For a ratio below 2, a cylindrical approximation is more accurate. The bead-to-wire ratio for the thermocouples used in this study are 2.3 and 2.5 for the 190 and 170 μm junctions respectively. In absence of a purely quantitative method, the junction is qualified as a sphere from the optical image used to measure the junction diameter.

Thermocouple Junction

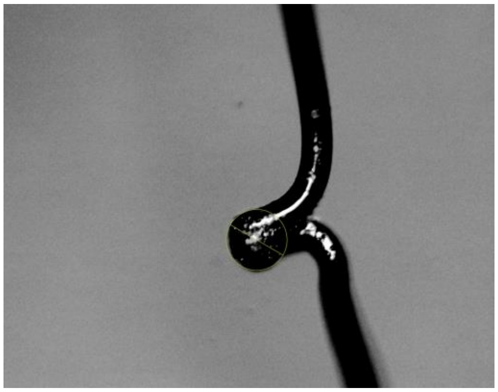

Figure A.15. Junction diameter measured by optical microscope. Observation of junction geometry assists in qualitative assessment. Arguments can be made for both a sphere and cylindrical shape. The sphere shape is chosen in part because it more closely reflects the observed hemispherical surface of the junction.